

A HIGH-ORDER UNSTAGGERED CONSTRAINED TRANSPORT METHOD FOR THE 3D IDEAL MAGNETOHYDRODYNAMIC EQUATIONS BASED ON THE METHOD OF LINES

CHRISTIANE HELZEL*, JAMES A. ROSSMANITH†, AND BERTRAM TAETZ‡

Abstract. Numerical methods for solving the ideal magnetohydrodynamic (MHD) equations in more than one space dimension must confront the challenge of controlling errors in the discrete divergence of the magnetic field. One approach that has been shown successful in stabilizing MHD calculations are constrained transport (CT) schemes. CT schemes can be viewed as predictor-corrector methods for updating the magnetic field, where a magnetic field value is first predicted by a method that does not exactly preserve the divergence-free condition on the magnetic field, followed by a correction step that aims to control these divergence errors. In Helzel et al. [*J. Comp. Phys.* **227**, 9527 (2011)] the authors presented an unstaggered constrained transport method for the MHD equations on three-dimensional Cartesian grids. In this approach an evolution equation for the magnetic potential is solved during each time step and a divergence-free update of the magnetic field is computed by taking the curl of the magnetic potential. The evolution equation for the vector potential is only weakly hyperbolic, which requires special numerical treatment. A key step in this method is the use of dimensional splitting in order to overcome these difficulties.

In this work we generalize the method of [*J. Comp. Phys.* **227**, 9527 (2011)] in three important ways: (1) we remove the need for operator splitting by switching to an appropriate method of lines discretization and coupling this with a non-conservative finite volume method for the magnetic vector potential equation, (2) we increase the spatial and temporal order of accuracy of the entire method to third order, and (3) we develop the method so that it is applicable on both Cartesian and logically rectangular mapped grids. The method of lines approach that is used in this work is based on a third-order accurate finite volume discretization in space coupled to a third order strong stability preserving Runge-Kutta time stepping method. The evolution equation for the magnetic vector potential is solved using a non-conservative finite volume method based on the approach of Castro et al. [*Math. Comput.* **79**, 1427 (2010)]. The curl of the magnetic potential is computed via a third-order accurate discrete operator that is derived from appropriate application of the divergence theorem and subsequent numerical quadrature on element faces. Special artificial resistivity limiters are used to control unphysical oscillations in the magnetic potential and field components across shocks. Several test computations are shown that confirm third order accuracy for smooth test problems and high-resolution for test problems with shock waves.

Key words. Magnetohydrodynamics, Constrained Transport, Hyperbolic Conservation Laws, Finite Volume Methods, Plasma Physics

AMS subject classifications. 35L02, 65M08, 65M20, 76N15

1. Introduction. It is well known that numerical methods for the multi-dimensional magnetohydrodynamic (MHD) equations must in some way respect the divergence-free condition on the magnetic field; failure to control divergence errors have been shown to lead to nonlinear numerical instabilities (e.g., see Tóth [42] for a discussion). Brackbill and Barnes [9] were one of the first to document this problem; since their paper a variety of approaches have been proposed to control the divergence of the magnetic field. The four main approaches that have been developed are 8-wave [36, 37], projection [3, 42], divergence-cleaning [18], and constrained transport methods [2, 4, 17, 20, 21, 26, 30, 31, 39, 40, 41, 42, 45]. We will not endeavor to provide a detailed description of these four numerical approaches, since such a

*Department of Mathematics, Ruhr-University Bochum, Universitätsstr. 150, 44780 Bochum, Germany (Christiane.Helzel@ruhr-uni-bochum.de)

†Department of Mathematics, Iowa State University, 396 Carver Hall, Ames, IA 50011, USA (rossmani@iastate.edu)

‡Department of Mathematics, Ruhr-University Bochum, Universitätsstr. 150, 44780 Bochum, Germany (Bertram.Taetz@rub.de)

description already exists in Tóth [42] and Helzel et al. [26]. Instead, because in this work we will develop a constrained transport method, we very briefly describe the CT methodology for MHD in the remainder of this section.

The basic framework of the constrained transport methodology was developed by Evans and Hawley [20]. The premise was to modify the celebrated Yee scheme [48] from vacuum electromagnetism to the ideal MHD equations; this framework included staggered electric and magnetic fields, just as in the Yee scheme. The resulting method can be viewed as predictor-corrector approach for updating the magnetic field, where a magnetic field value is first predicted by a method that does not exactly preserve the divergence-free condition on the magnetic field, followed by a correction step that aims to control these divergence errors. The basic steps in the Evans and Hawley CT approach can be outlined as follows:

- Step 0.** Start with MHD cell average values at the current time: $(\rho^n, \rho \mathbf{u}^n, \mathcal{E}^n, \mathbf{B}^n)$.
- Step 1.** Take a time-step using some finite volume method, which produces the cell average values: $(\rho^{n+1}, \rho \mathbf{u}^{n+1}, \mathcal{E}^{n+1}, \mathbf{B}^*)$. \mathbf{B}^* is the *predicted* value of the magnetic field.
- Step 2.** Using the ideal Ohm's law relationship, $\mathbf{E} = \mathbf{B} \times \mathbf{u}$, and some space and time interpolation scheme for \mathbf{B} and \mathbf{u} , reconstruct a space and time staggered electric field value: $\mathbf{E}^{n+\frac{1}{2}}$.
- Step 3.** Produce the *corrected* magnetic field value, \mathbf{B}^{n+1} , from the Yee scheme [48] step for the magnetic field:

$$\mathbf{B}^{n+1} = \mathbf{B}^n - \Delta t \nabla \times \mathbf{E}^{n+\frac{1}{2}},$$

where the curl operation is understood to be a discrete curl.

An alternative, but completely equivalent, interpretation of this scheme replaces **Step 3** above with the following:

- Step 3a.** Produce the magnetic potential value, \mathbf{A}^{n+1} , from the induction equation written in potential form:

$$\mathbf{A}^{n+1} = \mathbf{A}^n - \Delta t \mathbf{E}^{n+\frac{1}{2}}.$$

- Step 3b.** Produce the *corrected* magnetic field value, \mathbf{B}^{n+1} , by computing the discrete curl of the magnetic potential:

$$\mathbf{B}^{n+1} = \nabla \times \mathbf{A}^{n+1}.$$

By altering how **Step 2** (i.e., the reconstruction of the electric field) is done in the Evans and Hawley framework, a variety of CT schemes were developed, including Balsara and Spicer [4], Dai and Woodward [17], Ryu et al. [40], and Londrillo and Del Zanna [30, 31]. In his review article, Tóth [42] showed that constrained transport methods could also be formulated without the use of staggered electric and magnetic fields. Several of these unstaggered variants have been formulated, including the schemes of Fey and Torrilhon [21], Helzel et al. [26], and Rossmannith [39].

The particular focus of this work is to consider modifications of the constrained transport approaches of Rossmannith [39] and Helzel et al. [26]. Rossmannith [39] developed an unstaggered constrained transport method for the two-dimensional MHD equations on Cartesian grids. In this approach LeVeque's wave propagation method [28, 29] is used to update the conserved variables of the MHD equations. **Step 3a** of the CT framework is modified by directly solving a scalar transport equation for the out-of-plane magnetic potential:

$$A_{,t}^3 + u^1 A_{,x}^3 + u^2 A_{,y}^3 = 0. \tag{1.1}$$

The magnetic field components are computed via the curl operation on the magnetic potential:

$$B^1 = A^3_{,y} \quad \text{and} \quad B^2 = -A^3_{,x}. \quad (1.2)$$

Transport equation (1.1) for the potential is solved using a modified version of LeVeque’s wave propagation algorithm. In particular, the flux limiters of the wave propagation method are modified in the numerical solution of (1.1) in order to avoid not only unphysical oscillations in the magnetic potential but also in derivatives of the potential (i.e., the magnetic field).

Helzel et al. [26] extended this unstaggered constrained transport method to the three-dimensional MHD equations. In this case one has to consider the following transport equation for the vector potential:

$$\begin{aligned} \begin{bmatrix} A^1 \\ A^2 \\ A^3 \end{bmatrix}_{,t} + \begin{bmatrix} 0 & -u^2 & -u^3 \\ 0 & u^1 & 0 \\ 0 & 0 & u^1 \end{bmatrix} \begin{bmatrix} A^1 \\ A^2 \\ A^3 \end{bmatrix}_{,x} + \begin{bmatrix} u^2 & 0 & 0 \\ -u^1 & 0 & -u^3 \\ 0 & 0 & u^2 \end{bmatrix} \begin{bmatrix} A^1 \\ A^2 \\ A^3 \end{bmatrix}_{,y} \\ + \begin{bmatrix} u^3 & 0 & 0 \\ 0 & u^3 & 0 \\ -u^1 & -u^2 & 0 \end{bmatrix} \begin{bmatrix} A^1 \\ A^2 \\ A^3 \end{bmatrix}_{,z} = - \begin{bmatrix} \psi_{,x} \\ \psi_{,y} \\ \psi_{,z} \end{bmatrix}. \end{aligned} \quad (1.3)$$

The magnetic field components are computed via the curl operation on the magnetic potential:

$$B^1 = A^3_{,y} - A^2_{,z}, \quad B^2 = A^1_{,z} - A^3_{,x}, \quad \text{and} \quad B^3 = A^2_{,x} - A^1_{,y}. \quad (1.4)$$

In contrast to the 2D case, the 3D transport equation for the magnetic potential needs an additional constraint (i.e., the gauge condition) in order to get a closed set of evolution equations for the vector potential \mathbf{A} and the scalar potential ψ . Helzel et al. [26] chose the so-called Weyl gauge ($\psi \equiv 0$), which results in a transport equation for the vector potential that is only weakly hyperbolic. This means that standard methods for hyperbolic problems that are based on an eigenvector decomposition of the jump of the advected quantities at grid cell interfaces cannot be used. In order to overcome this difficulty, Helzel et al. [26] developed a second order accurate dimensional split method for the magnetic vector potential equation that is well defined also in the weakly hyperbolic case. Many test computations confirmed that this approach leads to a robust and accurate approximation of the MHD equations on Cartesian grids. For smooth solutions of the MHD equations, the method from [26] was shown to be second order accurate.

The focus of this work is to generalize the approach [26] in three important ways:

1. We remove the need for operator splitting by switching to an appropriate method of lines discretization and coupling this with a non-conservative finite volume method for the magnetic vector potential equation.
2. We increase the spatial and temporal order of accuracy of the entire method to third order using a third-order SSP-RK time-stepping method and a third-order finite volume spatial discretization.
3. We develop the method so that it is applicable on both Cartesian and logically rectangular mapped grids.

The nonconservative method that we use on the magnetic vector potential equation is inspired by previous work on the approximation of non-conservative hyperbolic systems by Canestrelli et al. [12], Dumbser et al. [19], and Ketcheson et al. [27]. By using a method of lines approach with a strong stability preserving Runge-Kutta (SSP-RK) method in time and third order accurate reconstruction in space, we are able to construct a third order accurate unstaggered

constrained transport method. In this approach, the correction of the magnetic field is performed during each stage of the Runge-Kutta method. For the spatial discretization we use a multidimensional (limited) polynomial reconstruction of the cell average quantities.

After a brief review of the ideal MHD equations in Section 2, we introduce the proposed constrained transport scheme in a series of four sections. In Section 3 we outline the time discretization of the proposed method and show how to embed the constrained transport steps into the various stages of the third-order SSP Runge-Kutta scheme. In Section 4 we describe the third order accurate spatial discretization for the MHD system. In Section 5 we show how to modify this approach to obtain a high-order non-conservative spatial discretization of the magnetic vector potential equation. In this section we also develop special artificial resistivity limiters that are used to control unphysical oscillations in both the magnetic potential and magnetic field components. In Section 6 we show how to compute the curl to high-order of the discrete magnetic vector potential. Several numerical examples on Cartesian and mapped grids are shown in Section 7; these examples are used to both verify the third-order accuracy in space and time, as well as the shock-capturing ability of the proposed scheme. Conclusions can be found in Section 8.

2. The ideal MHD equations. The ideal MHD equations are a first order hyperbolic system of conservation laws that can be written in the form

$$\frac{\partial}{\partial t} \begin{bmatrix} \rho \\ \rho \mathbf{u} \\ \mathcal{E} \\ \mathbf{B} \end{bmatrix} + \nabla \cdot \begin{bmatrix} \rho \mathbf{u} \mathbf{u} + \left(p + \frac{1}{2} \|\mathbf{B}\|^2\right) \mathbb{I} - \mathbf{B} \mathbf{B} \\ \mathbf{u} \left(\mathcal{E} + p + \frac{1}{2} \|\mathbf{B}\|^2\right) - \mathbf{B} (\mathbf{u} \cdot \mathbf{B}) \\ \mathbf{u} \mathbf{B} - \mathbf{B} \mathbf{u} \end{bmatrix} = 0, \quad (2.1)$$

$$\nabla \cdot \mathbf{B} = 0, \quad (2.2)$$

where ρ , $\rho \mathbf{u}$ and \mathcal{E} are the total mass, momentum and energy densities, and \mathbf{B} is the magnetic field. The thermal pressure, p , is related to the conserved quantities through the ideal gas law

$$p = (\gamma - 1) \left(\mathcal{E} - \frac{1}{2} \|\mathbf{B}\|^2 - \frac{1}{2} \rho \|\mathbf{u}\|^2 \right), \quad (2.3)$$

where $\gamma = 5/3$ is the ideal gas constant. Here $\|\cdot\|$ denotes the Euclidean vector norm. A complete derivation and discussion of MHD system (2.1)–(2.2) can be found in several standard plasma physics textbooks (e.g., [14, 23, 33]).

2.1. Hyperbolicity of the MHD system. We first note that system (2.1), along with the equation of state (2.3), provides a full set of equations for the time evolution of all eight state variables: $(\rho, \rho \mathbf{u}, \mathcal{E}, \mathbf{B})$. These evolution equations form a hyperbolic system. In particular, the eigenvalues of the flux Jacobian in some arbitrary direction \mathbf{n} ($\|\mathbf{n}\| = 1$) can be written as follows:

$$\lambda^{1,8} = \mathbf{u} \cdot \mathbf{n} \mp c_f : \text{fast magnetosonic waves}, \quad (2.4)$$

$$\lambda^{2,7} = \mathbf{u} \cdot \mathbf{n} \mp c_a : \text{Alfvén waves}, \quad (2.5)$$

$$\lambda^{3,6} = \mathbf{u} \cdot \mathbf{n} \mp c_s : \text{slow magnetosonic waves}, \quad (2.6)$$

$$\lambda^4 = \mathbf{u} \cdot \mathbf{n} : \text{entropy wave}, \quad (2.7)$$

$$\lambda^5 = \mathbf{u} \cdot \mathbf{n} : \text{divergence wave}, \quad (2.8)$$

where

$$a \equiv \sqrt{\frac{\gamma p}{\rho}}, \quad (2.9)$$

$$c_a \equiv \sqrt{\frac{(\mathbf{B} \cdot \mathbf{n})^2}{\rho}}, \quad (2.10)$$

$$c_f \equiv \left\{ \frac{1}{2} \left[a^2 + \frac{\|\mathbf{B}\|^2}{\rho} + \sqrt{\left(a^2 + \frac{\|\mathbf{B}\|^2}{\rho} \right)^2 - 4a^2 \frac{(\mathbf{B} \cdot \mathbf{n})^2}{\rho}} \right] \right\}^{1/2}, \quad (2.11)$$

$$c_s \equiv \left\{ \frac{1}{2} \left[a^2 + \frac{\|\mathbf{B}\|^2}{\rho} - \sqrt{\left(a^2 + \frac{\|\mathbf{B}\|^2}{\rho} \right)^2 - 4a^2 \frac{(\mathbf{B} \cdot \mathbf{n})^2}{\rho}} \right] \right\}^{1/2}. \quad (2.12)$$

The eigenvalues are well-ordered in the sense that

$$\lambda^1 \leq \lambda^2 \leq \lambda^3 \leq \lambda^4 \leq \lambda^5 \leq \lambda^6 \leq \lambda^7 \leq \lambda^8. \quad (2.13)$$

The fast and slow magnetosonic waves are genuinely nonlinear, while the remaining waves are linearly degenerate. Note that the so-called *divergence-wave* has been made to travel at the speed $\mathbf{u} \cdot \mathbf{n}$ via the Godunov-Powell formulation [22, 36, 37], thus restoring Galilean invariance.

2.2. The role of $\nabla \cdot \mathbf{B} = 0$ in numerical discretizations. If the initial magnetic field is divergence-free, then under the evolution described by equation (2.1), the divergence-free condition is satisfied for all time. This makes (2.2) an *involution* [16]. Unfortunately, although (2.2) is an involution under the evolution of the exact MHD system, it is generally not an involution of the discretized MHD equations. Furthermore, it has been well-documented in the literature that the failure of numerical methods to control divergence errors can lead to nonlinear numerical instabilities [42].

Explanations for why the divergence errors lead to numerical instabilities have been considered from a few different points-of-view. We briefly review the two main explanations below.

1. Brackbill and Barnes [8] showed that if $\nabla \cdot \mathbf{B} \neq 0$, then the magnetic force,

$$\mathbf{F} = \nabla \cdot \left\{ \mathbf{B}\mathbf{B} - \frac{1}{2}\|\mathbf{B}\|^2 \mathbb{I} \right\}, \quad (2.14)$$

in the direction of the magnetic field, will not in general vanish:

$$\mathbf{F} \cdot \mathbf{B} = \|\mathbf{B}\|^2 (\nabla \cdot \mathbf{B}) \neq 0. \quad (2.15)$$

If this spurious forcing becomes too large, it can lead to numerical instabilities [8, 39, 42].

2. Barth [7] gave an explanation based on the well-known result of Godunov [22] that the MHD entropy density,

$$U(q) = -\rho \log(p\rho^{-\gamma}), \quad (2.16)$$

produces a set of *entropy variables*, $v = U_{,q}$, that do not immediately symmetrize the ideal MHD equations. Instead, a symmetric hyperbolic form of ideal MHD can

only be obtained if an additional term that is proportional to the divergence of the magnetic field is included in the MHD equations:

$$\underbrace{q_{,t} + \nabla \cdot \mathbf{F}(q)}_{\text{ideal MHD}} + \underbrace{\chi_{,v} \nabla \cdot \mathbf{B}}_{\text{additional term}} = 0, \quad \text{where} \quad \chi(q) = (\gamma - 1) \frac{\rho \mathbf{u} \cdot \mathbf{B}}{p}. \quad (2.17)$$

By looking at how the entropy behaves on the discrete level, Barth [7] was able to prove that certain discontinuous Galerkin discretizations of the ideal MHD equations could be made to be *entropy stable* (see Tadmor [43]) if the discrete magnetic field was made globally divergence-free. The implication of this result is that schemes that do not control errors in the divergence of the magnetic field run the risk of becoming entropy unstable.

2.3. The evolution of the magnetic potential. Since the magnetic field is divergence-free, it can be written as the curl of a magnetic vector potential:

$$\mathbf{B} = \nabla \times \mathbf{A}. \quad (2.18)$$

The essential feature of constrained transport methods is to update the magnetic vector potential in some manner, and then by computing from it some discrete form of the curl, to obtain a discrete divergence-free magnetic field. Using the relation

$$\nabla \cdot (\mathbf{uB} - \mathbf{Bu}) = \nabla \times (\mathbf{B} \times \mathbf{u}),$$

the last row of (2.1) can be written in the form

$$\mathbf{B}_{,t} + \nabla \times (\mathbf{B} \times \mathbf{u}) = 0. \quad (2.19)$$

Since \mathbf{B} is divergence free, we set $\mathbf{B} = \nabla \times \mathbf{A}$ and rewrite (2.19) as

$$\nabla \times \{\mathbf{A}_{,t} + (\nabla \times \mathbf{A}) \times \mathbf{u}\} = 0, \quad (2.20)$$

$$\implies \mathbf{A}_{,t} + (\nabla \times \mathbf{A}) \times \mathbf{u} = -\nabla \psi, \quad (2.21)$$

where ψ is an arbitrary scalar function. Different choices of ψ represent different *gauge condition* choices, see [26].

Our approach is based on the Weyl gauge, which means we take $\psi \equiv 0$. This results in an evolution equation for the vector potential is given by

$$\mathbf{A}_{,t} + (\nabla \times \mathbf{A}) \times \mathbf{u} = 0, \quad (2.22)$$

which can also be rewritten in quasilinear form as

$$\mathbf{A}_{,t} + N_1(\mathbf{u}) \mathbf{A}_{,x} + N_2(\mathbf{u}) \mathbf{A}_{,y} + N_3(\mathbf{u}) \mathbf{A}_{,z} = 0, \quad (2.23)$$

with

$$N_1 = \begin{bmatrix} 0 & -u^2 & -u^3 \\ 0 & u^1 & 0 \\ 0 & 0 & u^1 \end{bmatrix}, \quad N_2 = \begin{bmatrix} u^2 & 0 & 0 \\ -u^1 & 0 & -u^3 \\ 0 & 0 & u^2 \end{bmatrix}, \quad N_3 = \begin{bmatrix} u^3 & 0 & 0 \\ 0 & u^3 & 0 \\ -u^1 & -u^2 & 0 \end{bmatrix}. \quad (2.24)$$

The the flux Jacobian in some direction $\mathbf{n} = (n^1, n^2, n^3)^T$,

$$M(\mathbf{n}, \mathbf{u}) := n^1 N_1 + n^2 N_2 + n^3 N_3 = \begin{bmatrix} n^2 u^2 + n^3 u^3 & -n^1 u^2 & -n^1 u^3 \\ -n^2 u^1 & n^1 u^1 + n^3 u^3 & -n^2 u^3 \\ -n^3 u^1 & -n^3 u^2 & n^1 u^1 + n^2 u^2 \end{bmatrix}, \quad (2.25)$$

has real eigenvalues for all $\|\mathbf{n}\| = 1$, but for any nonzero velocity vector, \mathbf{u} , there exist directions \mathbf{n} , for which $M(\mathbf{n}, \mathbf{u})$ does not have a complete set of right eigenvectors. Therefore, system (2.23)–(2.24) is only *weakly hyperbolic* [26]. In order to see this weak hyperbolicity, we write the eigenvalues of matrix (2.25):

$$\lambda = \{0, \mathbf{n} \cdot \mathbf{u}, \mathbf{n} \cdot \mathbf{u}\}, \quad (2.26)$$

and the matrix of right eigenvectors:

$$R = \left[r^{(1)} \mid r^{(2)} \mid r^{(3)} \right] = \begin{bmatrix} n^1 & n^2 u^3 - n^3 u^2 & u^1 (\mathbf{u} \cdot \mathbf{n}) - n^1 \|\mathbf{u}\|^2 \\ n^2 & n^3 u^1 - n^1 u^3 & u^2 (\mathbf{u} \cdot \mathbf{n}) - n^2 \|\mathbf{u}\|^2 \\ n^3 & n^1 u^2 - n^2 u^1 & u^3 (\mathbf{u} \cdot \mathbf{n}) - n^3 \|\mathbf{u}\|^2 \end{bmatrix}. \quad (2.27)$$

Assuming that $\|\mathbf{u}\| \neq 0$ and $\|\mathbf{n}\| = 1$, the determinant of matrix R can be written as

$$\det(R) = -\|\mathbf{u}\|^3 \cos(\alpha) \sin^2(\alpha), \quad (2.28)$$

where α is the angle between the vectors \mathbf{n} and \mathbf{u} . The difficulty is that for any non-zero velocity vector, \mathbf{u} , one can always find four directions, $\alpha = 0, \pi/2, \pi$, and $3\pi/2$, such that $\det(R) = 0$. In other words, for every $\|\mathbf{u}\| \neq 0$ there exists four degenerate directions in which the eigenvectors are incomplete.

3. Outline of the constrained transport algorithm and temporal discretization.

In our constrained transport method for the MHD equations, we separate the discretization in space and time. For the temporal discretization we use an SSP-RK method of order up to three, see e.g. [25, 24].

Consider a system of ordinary differential equations of the form

$$Q'(t) = \mathcal{L}(Q(t)). \quad (3.1)$$

One time step of the third order accurate SSP-RK method can be written in the form

$$\begin{aligned} Q^{(1)} &= Q^n + \Delta t \mathcal{L}(Q^n), \\ Q^{(2)} &= \frac{3}{4} Q^n + \frac{1}{4} Q^{(1)} + \frac{1}{4} \Delta t \mathcal{L}(Q^{(1)}), \\ Q^{n+1} &= \frac{1}{3} Q^n + \frac{2}{3} Q^{(2)} + \frac{2}{3} \Delta t \mathcal{L}(Q^{(2)}). \end{aligned} \quad (3.2)$$

In a method of lines approach we obtain systems of ordinary differential equations of the form (3.1) after discretizing the spatial derivatives. Here the components of the vector $Q(t)$ represent cell average values of the physical quantities in the different grid cells.

The semi-discrete form of (2.1) now has the form

$$Q'_{\text{MHD}}(t) = \mathcal{L}_1(Q_{\text{MHD}}(t)), \quad (3.3)$$

where $Q_{\text{MHD}}(t)$ represents the grid function at time t consisting of all cell averaged values of the conserved quantities from the MHD equations: $(\rho, \rho \mathbf{u}, \mathcal{E}, \mathbf{B})$. The precise form of the spatial discretization represented by $\mathcal{L}_1(Q_{\text{MHD}}(t))$ will be discussed in Section 4. The semi-discrete form of the evolution equation for the potential (2.22) has the general form

$$Q'_{\mathbf{A}}(t) = \mathcal{L}_2(Q_{\mathbf{A}}(t), Q_{\text{MHD}}(t)), \quad (3.4)$$

where $Q_{\mathbf{A}}(t)$ is the grid function at time t consisting of the cell averaged values of the magnetic vector potential, \mathbf{A} . Note that the evolution of the potential depends on the velocity field, which we take to be as given from the solution step of the MHD equation. This is reflected in the notation used in (3.4). The spatial discretization of the potential equation will be discussed in Section 5.

A single stage the constrained transport algorithm has the form:

0. Start with Q_{MHD}^n and $Q_{\mathbf{A}}^n$ (the solution from the previous time step) and $Q_{\text{MHD}}^{(k-1)}$ and $Q_{\mathbf{A}}^{(k-1)}$ (the solution from the previous time stage).
1. Update without regard to the divergence-free constraint on the magnetic field:

$$\begin{aligned} Q_{\text{MHD}}^{(k\star)} &= \alpha^{(k)} Q_{\text{MHD}}^n + (1 - \alpha^{(k)}) Q_{\text{MHD}}^{(k-1)} + \beta^{(k)} \Delta t \mathcal{L}_1 \left(Q_{\text{MHD}}^{(k-1)} \right), \\ Q_{\mathbf{A}}^{(k)} &= \alpha^{(k)} Q_{\mathbf{A}}^n + (1 - \alpha^{(k)}) Q_{\mathbf{A}}^{(k-1)} + \beta^{(k)} \Delta t \mathcal{L}_2 \left(Q_{\mathbf{A}}^{(k-1)}, Q_{\text{MHD}}^{(k-1)} \right), \end{aligned}$$

where $Q_{\text{MHD}}^{(k\star)} = (\rho^{(k)}, \rho \mathbf{u}^{(k)}, \mathcal{E}^{(k)}, \mathbf{B}^{(k\star)})$ and $\mathbf{B}^{(k\star)}$ denotes the *predicted* value of the magnetic field in the first Runge-Kutta stage.

2. The magnetic field components of $Q_{\text{MHD}}^{(k\star)}$ are then *corrected* by $\nabla \times Q_{\mathbf{A}}^{(k)}$:

$$\mathbf{B}^{(k)} = \nabla \times Q_{\mathbf{A}}^{(k)} \implies Q_{\text{MHD}}^{(k)} = \left(\rho^{(k)}, \rho \mathbf{u}^{(k)}, \mathcal{E}^{(k)}, \mathbf{B}^{(k)} \right).$$

For smooth solutions, this procedure with third-order accurate SSP-RK gives an update of the grid function Q_{MHD}^{n+1} that is 3rd order accurate in time. This fact is confirmed numerically via test computations done in Section 7.

Note that in each stage we take one Euler step on the magnetic vector potential equation (2.22). In each of these steps we evaluate the spatial discretization operator, \mathcal{L}_2 , at the current values of the potential, $Q_{\mathbf{A}}$, and the current velocity values that can be obtained from Q_{MHD} . Just as in the constrained transport approaches of [26, 39], during the Euler step on (2.22) we view the velocity \mathbf{u} as a given function, and view (2.22) as a closed equation for the magnetic potential \mathbf{A} .

4. Spatial discretization of the MHD equations. Our spatial discretization of the MHD equations is similar to the one used in SHARPCLAW by Ketcheson et al. [27]. However, in our method we use a multidimensional polynomial reconstruction. This gives the full order of convergence (here up to third order) for smooth nonlinear problems on Cartesian grids and reduces grid effects for non-smoothly varying mapped grids. We describe the one-dimensional, multidimensional Cartesian, and multidimensional mapped grid spatial discretizations in the subsequent three subsections.

4.1. One-dimensional spatial discretization. We first briefly discuss the one-dimensional case, where we consider a hyperbolic conservation law of the form

$$q_t + f(q)_{,x} = 0, \tag{4.1}$$

where $q : \mathbb{R}^+ \times \mathbb{R} \rightarrow \mathbb{R}^m$ is a vector of conserved quantities and $f : \mathbb{R}^m \rightarrow \mathbb{R}^m$ is the flux function. For smooth solutions we can transform (4.1) into the equivalent quasilinear form

$$q_t + A(q) q_x = 0, \tag{4.2}$$

where $A(q) := f_{,q}(q)$ is the flux Jacobian matrix ($A : \mathbb{R}^m \rightarrow \mathbb{R}^{m \times m}$). We assume that some initial data $q(0, x) = q_0(x)$ with $q_0 : \mathbb{R} \rightarrow \mathbb{R}^m$ and some appropriate boundary conditions are given.

The cell average of the conserved quantity in grid cell i at time t is denoted by $Q_i(t)$, i.e.

$$Q_i(t) \approx \frac{1}{\Delta x} \int_{x_{i-\frac{1}{2}}}^{x_{i+\frac{1}{2}}} q(t, x) dx. \quad (4.3)$$

From the given cell average values we compute piecewise polynomial approximations (with WENO limiting) of the conserved quantities, using polynomials of degree at most p . For smooth solutions these polynomial agree up to order p with the exact solution:

$$\begin{aligned} \tilde{q}(t^n, x) &:= \tilde{q}_i(t^n, x) \quad \text{for } x \in \left(x_{i-\frac{1}{2}}, x_{i+\frac{1}{2}}\right), \\ \tilde{q}_i(t^n, x) &= q(t^n, x) + \mathcal{O}(\Delta x^{p+1}). \end{aligned} \quad (4.4)$$

The reconstructed values from grid cell i at the left and right grid cell interface are denoted by

$$q_{i-\frac{1}{2}}^+ := \lim_{\varepsilon \rightarrow 0} \tilde{q}_i \left(x_{i-\frac{1}{2}} + \varepsilon\right) \quad \text{and} \quad q_{i+\frac{1}{2}}^- := \lim_{\varepsilon \rightarrow 0} \tilde{q}_i \left(x_{i+\frac{1}{2}} - \varepsilon\right). \quad (4.5)$$

In semi-discrete form, the method that is used to evolve the cell averages of the conserved quantities is given by (see [27])

$$Q'_i(t) = -\frac{1}{\Delta x} \left(\mathcal{A}^- \Delta q_{i+\frac{1}{2}} + \mathcal{A}^+ \Delta q_{i-\frac{1}{2}} + \mathcal{A} \Delta q_i \right). \quad (4.6)$$

The fluctuations $\mathcal{A}^\pm \Delta q_{i+\frac{1}{2}}$ can be computed as in the standard wave propagation algorithm of LeVeque [28], or by using the f -wave approach of Bale et al. [1], with the only difference being that the left and right values of the conserved quantities used in the wave decomposition or f -wave decomposition are obtained from the reconstructed interface values instead of the cell average values. The additional term

$$\mathcal{A} \Delta q_i = \int_{x_{i-\frac{1}{2}}}^{x_{i+\frac{1}{2}}} A(\tilde{q}_i) \tilde{q}_{i,x} dx \approx \int_{x_{i-\frac{1}{2}}}^{x_{i+\frac{1}{2}}} A(q) q_{,x} dx,$$

can be computed via Gaussian quadrature of the appropriate order. For the approximation of a hyperbolic problem in the flux difference form (4.1), the integral is equal to the flux difference:

$$\int_{x_{i-\frac{1}{2}}}^{x_{i+\frac{1}{2}}} A(\tilde{q}_i) \tilde{q}_{i,x} dx = f \left(q_{i+\frac{1}{2}}^- \right) - f \left(q_{i-\frac{1}{2}}^+ \right).$$

Furthermore, the fluctuations satisfy

$$\begin{aligned} \mathcal{A}^+ \Delta q_{i-\frac{1}{2}} &= f \left(q_{i-\frac{1}{2}}^+ \right) - f_{i-\frac{1}{2}}^* \left(q_{i-\frac{1}{2}}^-, q_{i-\frac{1}{2}}^+ \right), \\ \mathcal{A}^- \Delta q_{i+\frac{1}{2}} &= f_{i+\frac{1}{2}}^* \left(q_{i+\frac{1}{2}}^-, q_{i+\frac{1}{2}}^+ \right) - f \left(q_{i+\frac{1}{2}}^- \right). \end{aligned}$$

Here f^* denotes the interface flux, which is computed by solving a Riemann problem for the reconstructed left and right interface values. Thus for hyperbolic problems in divergence form, the method can be formulated as a finite volume method of the form

$$Q'_i(t) = \frac{1}{\Delta x} \left(f_{i+\frac{1}{2}}^* \left(q_{i+\frac{1}{2}}^-, q_{i+\frac{1}{2}}^+ \right) - f_{i-\frac{1}{2}}^* \left(q_{i-\frac{1}{2}}^-, q_{i-\frac{1}{2}}^+ \right) \right). \quad (4.7)$$

The Riemann problem can be solved using a variety of solvers; as a matter of practice, in this work we use the Roe-type Riemann solvers of the form described in Bale et al. [1].

4.2. Multidimensional Cartesian grids. For simplicity, we consider a two-dimensional hyperbolic equation of the form

$$q_{,t} + f(q)_{,x} + g(q)_{,y} = 0, \quad (4.8)$$

or of the quasilinear form

$$q_{,t} + A(q) q_{,x} + B(q) q_{,y} = 0. \quad (4.9)$$

Here $q : \mathbb{R}^+ \times \mathbb{R}^2 \rightarrow \mathbb{R}^m$ is a vector of conserved quantities, $f, g : \mathbb{R}^m \rightarrow \mathbb{R}^m$ are numerical flux functions, and $A(q) = f'(q)$, $B(q) = g'(q)$ are the flux Jacobian matrices.

In order to get a high-order accurate approximation in space with the method of lines approach, we need to reconstruct values on cell interfaces at nodes of a quadrature formula that is used to approximate interface fluxes (or fluctuations). In order to do this, we compute a piecewise polynomial reconstruction \tilde{q} of the conserved quantities in each grid cell. The grid cell average of this reconstructed polynomial agrees with the original cell average (this is needed to guarantee numerical conservation). Furthermore, the reconstruction is based on a (limited) least squares approach that includes all neighbors that share an edge or a corner with the considered grid cell, see [5, 44, 46].

The numerical method can be written as a finite volume scheme in the semi-discrete form

$$Q'_{ij}(t) = -\frac{1}{\Delta x} \left(f_{i+\frac{1}{2}j}^* - f_{i-\frac{1}{2}j}^* \right) - \frac{1}{\Delta y} \left(g_{ij+\frac{1}{2}}^* - g_{ij-\frac{1}{2}}^* \right), \quad (4.10)$$

or in the form used by the wave propagation algorithm (compare with [27])

$$\begin{aligned} Q'_{ij}(t) = & \frac{1}{\Delta x} \left(\mathcal{A}^+ \Delta q_{i-\frac{1}{2}j} + \mathcal{A}^- \Delta q_{i+\frac{1}{2}j} + \mathcal{A} \Delta q_{ij} \right) \\ & + \frac{1}{\Delta y} \left(\mathcal{B}^+ \Delta q_{ij-\frac{1}{2}} + \mathcal{B}^- \Delta q_{ij+\frac{1}{2}} + \mathcal{B} \Delta q_{ij} \right). \end{aligned} \quad (4.11)$$

Now $Q_{ij}(t)$ is an approximation of the cell average of the conserved quantity at time t in grid cell (i, j) . Using the piecewise polynomial reconstruction of the conserved quantity q in each grid cell, we can evaluate left and right values of the conserved quantity at Gaussian quadrature points along grid cell interfaces. These are used to obtain a high order accurate representation of the flux:

$$\frac{1}{\Delta y} \int_{y_{j-\frac{1}{2}}}^{y_{j+\frac{1}{2}}} f^* \left(q \left(x_{i\pm\frac{1}{2}}, y \right) \right) dy \approx \frac{1}{\Delta y} \sum_{k=1}^q c_k f^* \left(q_{i\pm\frac{1}{2}j_k}^-, q_{i\pm\frac{1}{2}j_k}^+ \right) =: f_{i\pm\frac{1}{2}j}^*, \quad (4.12)$$

$$\frac{1}{\Delta x} \int_{x_{i-\frac{1}{2}}}^{x_{i+\frac{1}{2}}} g^* \left(q \left(x, y_{j\pm\frac{1}{2}} \right) \right) dx \approx \frac{1}{\Delta x} \sum_{k=1}^q c_k g^* \left(q_{i_kj\pm\frac{1}{2}}^-, q_{i_kj\pm\frac{1}{2}}^+ \right) =: g_{ij\pm\frac{1}{2}}^*. \quad (4.13)$$

The coefficients c_k are the quadrature weights and x_{i_k} and y_{j_k} are the quadrature points. In an analogous way we can define the fluctuations $\mathcal{A}^\pm \Delta q$ and $\mathcal{B}^\pm \Delta q$ along a grid cell interface.

In order to compute the flux values f^* and g^* at the Gaussian quadrature points on the cell interface, we use a Roe-type Riemann solver of the form described in Bale et al. [1]. An advantage of this Riemann solver over the classical Roe solver is that Roe averages can be replaced with simpler averages; this feature is very helpful in the case of the MHD equations. In any Roe-type solver, we are required to compute right and left eigenvectors of the flux Jacobian; for the MHD system one has to be careful about the eigenvector scalings in order to

avoid singularities in the eigenvector basis [38]. For the MHD system we use the eigenvectors proposed by Barth [6, pages 212–214], which are based on the entropy variables and have near optimal scaling properties for physically admissible solution values.

We have shown here only the 2D spatial discretization. We omit the details of the 3D spatial discretization, since the extension to 3D is straightforward. In 3D we use a three-dimensional limited piecewise polynomial reconstruction of the conserved quantities and the fluxes at grid cell interfaces are computed by integration over a rectangular area (i.e., a surface integral instead of a line integral as in 2D).

4.3. Mapped grids. The spatial discretization can also be extended to two-dimensional logically rectangular mapped grids and three-dimensional hexahedral grids. The vertices of each mapped grid cell in physical space, (x, y, z) , are obtained by mapping the vertices from a Cartesian mesh in computational space, (ξ, η, ζ) (see [11]).

In three space dimensions, each grid cell can be represented by a trilinear map (also called a ruled cell) [10, 47] of the form

$$\mathbf{X}(\xi, \eta, \zeta) = c_{000} + c_{100}\xi + c_{010}\eta + c_{001}\zeta + c_{110}\xi\eta + c_{101}\xi\zeta + c_{011}\eta\zeta + c_{111}\xi\eta\zeta,$$

where $\mathbf{X} = (x, y, z)$, $0 \leq \xi, \eta, \zeta \leq 1$, and $c_{000}, \dots, c_{111} \in \mathbb{R}^3$ are vector coefficients. The coefficients are determined from the vertices of the hexahedral cell. This representation of the grid cell can be used to compute the volume of each grid cell, as well as face areas of all the faces, and the unit normal vectors at each face. The two-dimensional case is obtained by setting $\zeta = 0$.

Consider a multidimensional hyperbolic system of the general form

$$q_t + \nabla \cdot \mathbf{F} = 0,$$

where the columns of the matrix $\mathbf{F} = [f|g|h]$ are the flux functions in the x , y and z direction. We consider the semi-discrete form of the finite volume method for a three-dimensional grid cell that we denote C_{ijk} . The volume of the grid cell in physical space is denoted by $|C_{ijk}|$. This volume can be computed using the Jacobian determinant of the trilinear map

$$|C_{ijk}| = \int_0^1 \int_0^1 \int_0^1 \left| \frac{\partial \mathbf{X}}{\partial (\xi, \eta, \zeta)} \right| d\xi d\eta d\zeta. \quad (4.14)$$

Formulas to evaluate this expression are given in [47].

The change of the cell average of the conserved quantity in grid cell (i, j, k) is described by

$$Q'_{ijk}(t) = -\frac{1}{|C_{ijk}|} \iiint_{C_{ijk}} \nabla \cdot \mathbf{F} dV = -\frac{1}{|C_{ijk}|} \oint_{\partial C_{ijk}} \mathbf{F} \cdot \nu dA, \quad (4.15)$$

where ν is the outward pointing normal vector along the outer boundary of the grid cell.

At each face of a three-dimensional grid cell, one of the variables ξ, η, ζ is either zero or one and the face is represented by a ruled surface. Consider for example the grid cell face that corresponds to $\zeta = 0$ in computational space (this is the interface with the index $(i, j, k - \frac{1}{2})$). In physical space, this interface is described by the bilinear map

$$\mathbf{X}(\xi, \eta) = c_{00} + c_{10}\xi + c_{01}\eta + c_{11}\xi\eta,$$

which maps a square in computational space to a ruled surface embedded in \mathbb{R}^3 . In order to further describe this grid cell interface we define vectors

$$\mathbf{t}_{(1)} = \frac{\partial \mathbf{X}}{\partial \xi} = c_{10} + c_{11}\eta, \quad \mathbf{t}_{(2)} = \frac{\partial \mathbf{X}}{\partial \eta} = c_{01} + c_{11}\xi,$$

which are tangent vectors to coordinate lines. The surface metric tensor $(a_{ij})_{i,j=1,2}$ is defined as

$$a_{ij} = \mathbf{t}_{(i)} \cdot \mathbf{t}_{(j)}, \quad i, j, = 1, 2, \quad (4.16)$$

and $a = a_{11}a_{22} - a_{12}a_{21}$ denotes the determinant of the metric tensor. The unit normal vector to the grid cell interface can be computed using

$$\mathbf{n}(\xi, \eta) = \frac{\mathbf{t}_{(1)} \times \mathbf{t}_{(2)}}{\|\mathbf{t}_{(1)} \times \mathbf{t}_{(2)}\|}. \quad (4.17)$$

Note that with this definition, $\mathbf{n}_{i-\frac{1}{2},j,k}$ is an outward pointing normal vector for grid cell $(i-1, j, k)$ and an inward pointing normal vector for cell (i, j, k) , compare with the signs of the terms in equation (4.19).

The area element dA on the grid cell interface transforms according to

$$dA = \sqrt{a} d\xi d\eta = \|\mathbf{t}_{(1)} \times \mathbf{t}_{(2)}\| d\xi d\eta. \quad (4.18)$$

Note that the surface normal vector \mathbf{n} and the determinant a are functions of ξ and η . Analogously we can express the area element and a normal vector at all other grid cell interfaces. Using this, we can express (4.15) in computational space by

$$\begin{aligned} Q'_{ijk}(t) = \frac{-1}{|C'_{ijk}|} & \left[\int_0^1 \int_0^1 \left\{ \left(\mathbf{F} \cdot \mathbf{n}(\eta, \zeta) \sqrt{a(\eta, \zeta)} \right)_{i+\frac{1}{2}jk} - \left(\mathbf{F} \cdot \mathbf{n}(\eta, \zeta) \sqrt{a(\eta, \zeta)} \right)_{i-\frac{1}{2}jk} \right\} d\eta d\zeta \right. \\ & + \int_0^1 \int_0^1 \left\{ \left(\mathbf{F} \cdot \mathbf{n}(\xi, \zeta) \sqrt{a(\xi, \zeta)} \right)_{ij+\frac{1}{2}k} - \left(\mathbf{F} \cdot \mathbf{n}(\xi, \zeta) \sqrt{a(\xi, \zeta)} \right)_{ij-\frac{1}{2}k} \right\} d\xi d\zeta \\ & \left. + \int_0^1 \int_0^1 \left\{ \left(\mathbf{F} \cdot \mathbf{n}(\xi, \eta) \sqrt{a(\xi, \eta)} \right)_{ijk+\frac{1}{2}} - \left(\mathbf{F} \cdot \mathbf{n}(\xi, \eta) \sqrt{a(\xi, \eta)} \right)_{ijk-\frac{1}{2}} \right\} d\xi d\eta \right]. \end{aligned} \quad (4.19)$$

We integrate over grid cell interfaces in computational space using two-dimensional quadrature rules. The flux computation normal to the interface is again based on an approximative Riemann solver using the eigenvector decomposition of Barth.

5. Spatial discretization of the non-conservative magnetic vector potential equation. In this section we discuss the spatial discretization that is used to approximate the evolution equation for the magnetic potential. For the 2D ideal MHD equations the relevant scalar evolution equation for the magnetic potential is (1.1), while in 3D the relevant weakly hyperbolic system is (2.23)–(2.24). Just as in the previous section, we introduce the basic features of the numerical scheme for a one-dimensional problem.

5.1. One-dimensional weakly hyperbolic systems. We consider an equation of the general form

$$q_{,t} + A(x)q_{,x} = 0, \quad (5.1)$$

with $q : \mathbb{R}^+ \times \mathbb{R} \rightarrow \mathbb{R}^m$ and $A(x) \in \mathbb{R}^{m \times m}$. We assume that system (5.1) is weakly hyperbolic, which means that matrix $A(x)$ has real eigenvalues but not always a complete set of right eigenvectors. As in the classical hyperbolic case, we wish to construct a method of the form (4.6). However, due to the weak hyperbolicity, the fluctuations $\mathcal{A}^\pm \Delta q$ cannot be approximated via a wave decomposition as in [1, 27, 28].

Let \tilde{q} be a piecewise polynomial reconstruction of the function q as described in (4.4). Furthermore, let $\tilde{A}(x)$ denote a piecewise polynomial approximation of the matrix $A(x)$:

$$\begin{aligned}\tilde{A}(x) &= \tilde{A}_i(x) \quad \text{for } x \in \left(x_{i-\frac{1}{2}}, x_{i+\frac{1}{2}}\right), \\ \tilde{A}_i(x) &= A(x) + \mathcal{O}(\Delta x^{p+1}).\end{aligned}\tag{5.2}$$

The values $q_{i-\frac{1}{2}}^\pm$ are the reconstructed values at the grid cell interface as defined in (4.5). Analogously we define

$$A_{i-\frac{1}{2}}^- := \lim_{\varepsilon \rightarrow 0} \tilde{A}_{i-1} \left(x_{i-\frac{1}{2}} - \varepsilon\right) \quad \text{and} \quad A_{i-\frac{1}{2}}^+ := \lim_{\varepsilon \rightarrow 0} \tilde{A}_i \left(x_{i-\frac{1}{2}} + \varepsilon\right).\tag{5.3}$$

Using these reconstructions, we derive a method of the form

$$Q_i'(t) = -\frac{1}{\Delta x} \left(\mathcal{A}^- \Delta q_{i+\frac{1}{2}} + \mathcal{A}^+ \Delta q_{i-\frac{1}{2}} + \mathcal{A} \Delta q_i \right),$$

where $Q_i(t)$ is the cell average of the quantity q and

$$\mathcal{A} \Delta q_i \approx \lim_{\varepsilon \rightarrow 0} \int_{x_{i-\frac{1}{2}} + \varepsilon}^{x_{i+\frac{1}{2}} - \varepsilon} A(x) q_x dx,\tag{5.4}$$

$$\mathcal{A}^+ \Delta q_{i-1/2} \approx \lim_{\varepsilon \rightarrow 0} \int_{x_{i-1/2}}^{x_{i-1/2} + \varepsilon} A(x) q_x dx,\tag{5.5}$$

$$\mathcal{A}^- \Delta q_{i+1/2} \approx \lim_{\varepsilon \rightarrow 0} \int_{x_{i+1/2} - \varepsilon}^{x_{i+1/2}} A(x) q_x dx.\tag{5.6}$$

The integral in (5.4) is approximated by replacing $A(x)$ and q by the approximating polynomials \tilde{A}_i and \tilde{q}_i , i.e.

$$\mathcal{A} \Delta q_i := \int_{x_{i-\frac{1}{2}}}^{x_{i+\frac{1}{2}}} \tilde{A}_i(x) \tilde{q}_{i,x} dx.$$

This integral can then be computed using Gaussian quadrature of the appropriate order.

In the weakly hyperbolic case, the fluctuations $\mathcal{A}^\pm \Delta q$ cannot be computed with the wave propagation algorithm, since the wave propagation method requires a complete set of eigenvectors. In order to compute these fluctuations, we introduce a regularization of q at each grid cell interface of the form

$$q_{i-\frac{1}{2}}^\varepsilon(t, x) = \begin{cases} q_{i-\frac{1}{2}}^-(t) & : & x \leq x_{i-\frac{1}{2}} - \varepsilon, \\ \Psi_{i-\frac{1}{2}} \left(\frac{x - x_{i-\frac{1}{2}} + \varepsilon}{2\varepsilon}, t \right) & : & x \in \left(x_{i-\frac{1}{2}} - \varepsilon, x_{i-\frac{1}{2}} + \varepsilon \right), \\ q_{i-\frac{1}{2}}^+(t) & : & x \geq x_{i-\frac{1}{2}} + \varepsilon, \end{cases}$$

where $\Psi_{i-\frac{1}{2}}$ is a path connecting $q_{i-\frac{1}{2}}^-(t)$ and $q_{i-\frac{1}{2}}^+(t)$. Using this regularization, we first construct an expression for the sum of the left and right-going fluctuations at the grid cell interface $x_{i-\frac{1}{2}}$, i.e., we wish to express

$$\mathcal{A}^- \Delta q_{i-\frac{1}{2}} + \mathcal{A}^+ \Delta q_{i-\frac{1}{2}} \approx \lim_{\varepsilon \rightarrow 0} \int_{x_{i-\frac{1}{2}} - \varepsilon}^{x_{i-\frac{1}{2}} + \varepsilon} A(x) q_x dx.$$

This integral is approximated by replacing q with the regularized function q^ε and by replacing the matrix A with the piecewise polynomial approximation $\tilde{A}(x)$, i.e., we set

$$\mathcal{A}^- \Delta q_{i-\frac{1}{2}} + \mathcal{A}^+ \Delta q_{i-\frac{1}{2}} = \lim_{\varepsilon \rightarrow 0} \int_{x_{i-\frac{1}{2}} - \varepsilon}^{x_{i-\frac{1}{2}} + \varepsilon} \tilde{A}(x) \left(q_{i-\frac{1}{2}}^\varepsilon(t, x) \right)_{,x} dx. \quad (5.7)$$

After the substitution $s = \frac{x - x_{i-\frac{1}{2}} + \varepsilon}{2\varepsilon}$ and by defining $\phi(s) := x_{i-\frac{1}{2}} - \varepsilon + s(x_{i-\frac{1}{2}} + \varepsilon - (x_{i-\frac{1}{2}} - \varepsilon))$, the integral in (5.7) can be written as

$$\int_{x_{i-\frac{1}{2}} - \varepsilon}^{x_{i-\frac{1}{2}} + \varepsilon} \tilde{A}(x) \left(q_{i-\frac{1}{2}}^\varepsilon(t, x) \right)_{,x} dx = \int_0^1 \tilde{A}(\phi(s)) \left(\Psi_{i-\frac{1}{2}}(s, t) \right)_{,s} ds. \quad (5.8)$$

In order to resolve this integral, we choose the simple straight-line path

$$\Psi_{i-\frac{1}{2}} = q_{i-\frac{1}{2}}^- + s \left(q_{i-\frac{1}{2}}^+ - q_{i-\frac{1}{2}}^- \right), \quad (5.9)$$

and obtain

$$\int_0^1 \tilde{A}(\phi(s)) \left(\Psi_{i-\frac{1}{2}}(s, t) \right)_{,s} ds = \int_0^1 \tilde{A}(\phi(s)) ds \left(q_{i-\frac{1}{2}}^+(t) - q_{i-\frac{1}{2}}^-(t) \right). \quad (5.10)$$

The integral on the right-hand side can be split into two pieces:

$$\int_0^1 \tilde{A}(\phi(s)) ds = \int_0^{1/2} \tilde{A}_{i-1}(\phi(s)) ds + \int_{1/2}^1 \tilde{A}_i(\phi(s)) ds, \quad (5.11)$$

which corresponds to a division into pieces on the left and right of the discontinuity $x_{i-\frac{1}{2}}$. We then take the limit $\varepsilon \rightarrow 0$ and get:

$$\lim_{\varepsilon \rightarrow 0} \left(\int_0^{1/2} \tilde{A}_{i-1}(\phi(s)) ds + \int_{1/2}^1 \tilde{A}_i(\phi(s)) ds \right) = \frac{1}{2} A_{i-\frac{1}{2}}^- + \frac{1}{2} A_{i-\frac{1}{2}}^+ =: A|_{\Psi_{i-\frac{1}{2}}}. \quad (5.12)$$

Thus we obtain

$$\mathcal{A}^- \Delta q_{i-\frac{1}{2}} + \mathcal{A}^+ \Delta q_{i-\frac{1}{2}} = A|_{\Psi_{i-\frac{1}{2}}} (q_{i-\frac{1}{2}}^+ - q_{i-\frac{1}{2}}^-). \quad (5.13)$$

Following Castro et al. [13] and using relationship (5.13), we are now able to define the left and right-going fluctuations. With partial knowledge of the eigenstructure of $A|_{\Psi}$ (i.e., if we know the eigenvalues or an estimate of the largest absolute value of the eigenvalues) we can define

$$\mathcal{A}^- \Delta q_{i+1/2} = \frac{1}{2} \left[\underbrace{A|_{\Psi_{i+1/2}} - \alpha_{i+1/2} \mathbb{I}}_{\text{generalized Rusanov flux}} \right] \left(q_{i+\frac{1}{2}}^+ - q_{i+\frac{1}{2}}^- \right) \quad (5.14)$$

and

$$\mathcal{A}^+ \Delta q_{i-1/2} = \frac{1}{2} \left[\underbrace{A|_{\Psi_{i-1/2}} + \alpha_{i-1/2} \mathbb{I}}_{\text{generalized Rusanov flux}} \right] \left(q_{i-\frac{1}{2}}^+ - q_{i-\frac{1}{2}}^- \right), \quad (5.15)$$

where $\mathbb{I} \in \mathbb{R}^{m \times m}$ is the identity matrix. Here α is a positive number with

$$|\lambda^k| \leq \alpha, \quad \text{for } k = 1, \dots, m,$$

where λ^k represents the k^{th} eigenvalue of $A|_{\Psi}$, see [13].

Another possibility is to define the fluctuations without using any knowledge of the eigenstructure of $A|_{\Psi}$:

$$\mathcal{A}^- \Delta q_{i+1/2} = \frac{1}{4} \left[2A|_{\Psi_{i+\frac{1}{2}}} - \frac{\Delta x}{\Delta t} \mathbb{I} - \frac{\Delta t}{\Delta x} \left(A|_{\Psi_{i+\frac{1}{2}}} \right)^2 \right] \left(q_{i+\frac{1}{2}}^+ - q_{i+\frac{1}{2}}^- \right) \quad (5.16)$$

and

$$\mathcal{A}^+ \Delta q_{i-1/2} = \frac{1}{4} \left[2A|_{\Psi_{i-\frac{1}{2}}} + \frac{\Delta x}{\Delta t} \mathbb{I} + \frac{\Delta t}{\Delta x} \left(A|_{\Psi_{i-\frac{1}{2}}} \right)^2 \right] \left(q_{i-\frac{1}{2}}^+ - q_{i-\frac{1}{2}}^- \right). \quad (5.17)$$

These fluctuations are derived from the generalized FORCE scheme [12, 13], which is a convex combination of the generalized Lax-Friedrichs and the generalized Lax-Wendroff scheme.

5.2. Multidimensional Cartesian grids. We now consider the approximation of a weakly hyperbolic system of the form

$$q_t + A(x, y) q_x + B(x, y) q_y = 0, \quad (5.18)$$

with $q : \mathbb{R}^+ \times \mathbb{R}^2 \rightarrow \mathbb{R}^m$, $A(x, y)$, $B(x, y) \in \mathbb{R}^{m \times m}$. In the semi-discrete case, the method has the form

$$\begin{aligned} Q'_{ij}(t) = & -\frac{1}{\Delta x} \left(\mathcal{A}^+ \Delta q_{i-\frac{1}{2}j} + \mathcal{A}^- \Delta q_{i+\frac{1}{2}j} + \mathcal{A} \Delta q_{ij} \right) \\ & -\frac{1}{\Delta y} \left(\mathcal{B}^+ \Delta q_{i,j-\frac{1}{2}} + \mathcal{B}^- \Delta q_{i,j+\frac{1}{2}} + \mathcal{B} \Delta q_{ij} \right). \end{aligned} \quad (5.19)$$

As in the case of hyperbolic systems (see Section 4.2), we compute a multidimensional piecewise polynomial reconstruction \tilde{q} of q using a least squares approach. Furthermore, $\tilde{A}(x, y)$ and $\tilde{B}(x, y)$ are piecewise polynomial approximations of the matrix valued functions. Using these reconstructions we define

$$\begin{aligned} \mathcal{A} \Delta q_{ij} &:= \frac{1}{\Delta y} \int_{y_{j-\frac{1}{2}}}^{y_{j+\frac{1}{2}}} \int_{x_{i-\frac{1}{2}}}^{x_{i+\frac{1}{2}}} \tilde{A}_{ij}(x, y) \tilde{q}_{ij,x} dx dy, \\ \mathcal{B} \Delta q_{ij} &:= \frac{1}{\Delta x} \int_{y_{j-\frac{1}{2}}}^{y_{j+\frac{1}{2}}} \int_{x_{i-\frac{1}{2}}}^{x_{i+\frac{1}{2}}} \tilde{B}_{ij}(x, y) \tilde{q}_{ij,y} dx dy. \end{aligned} \quad (5.20)$$

The fluctuations \mathcal{A}^\pm and \mathcal{B}^\pm are defined in analogy to (5.14) and (5.15) with the only difference that we integrate over a grid cell interface and then compute the average value. For example, we compute

$$\mathcal{A}^- \Delta q_{i+\frac{1}{2}j} = \frac{1}{\Delta y} \int_{y_{j-\frac{1}{2}}}^{y_{j+\frac{1}{2}}} \frac{1}{2} \left[A|_{\Psi_{i+1/2j}}(y) - \alpha_{i+\frac{1}{2}}(y) \mathbb{I} \right] \left(q_{i+\frac{1}{2}j}^+(y) - q_{i+\frac{1}{2}j}^-(y) \right) dy. \quad (5.21)$$

We evaluate this integral using Gaussian quadrature formulas. This means that we need to compute the matrix $A|_{\Psi_{i+\frac{1}{2}j}}$ at the nodes of the quadrature formula. The other fluctuations are computed in an analogous way.

5.3. Mapped grids. We now discuss the discretization of a weakly hyperbolic system of the form (5.18) on a logically rectangular mapped grid. For simplicity we restrict our considerations to the two-dimensional case. The extension to the three-dimensional case is a combination of the concepts discussed in this section and those of Section 4.3.

Let C_{ij} denote a grid cell in physical space and $|C_{ij}|$ the area of the grid cell. Assume that the grid cell in physical space is obtained by a mapping of the unit square in computational space. The change of the cell average of the quantity q in grid cell C_{ij} is described by the ODE:

$$Q'_{ij}(t) = -\frac{1}{|C_{ij}|} \left(\ell_{i-\frac{1}{2}j} \mathcal{A}^+ \Delta q_{i-\frac{1}{2}j} + \tilde{A}_{ij} \tilde{q}_{ij,x} + \ell_{i+\frac{1}{2}j} \mathcal{A}^- \Delta q_{i+\frac{1}{2}j} \right. \\ \left. + \ell_{i,j-\frac{1}{2}} \mathcal{B}^+ \Delta q_{i,j-\frac{1}{2}} + \tilde{B}_{ij} \tilde{q}_{ij,y} + \ell_{i,j+\frac{1}{2}} \mathcal{B}^- \Delta q_{i,j+\frac{1}{2}} \right), \quad (5.22)$$

where $\ell_{i+\frac{1}{2}j}$ and $\ell_{i,j+\frac{1}{2}}$ denote the length of the grid cell interfaces in physical space. The integrals over the grid cell are defined as

$$\tilde{A}_{ij} \tilde{q}_{ij,x} = \iint_{C_{ij}} \tilde{A}_{ij}(x, y) \tilde{q}_{ij,x}(x, y) dx dy \\ = \int_0^1 \int_0^1 \sqrt{a_{ij}(\xi, \eta)} \tilde{A}_{ij}(x(\xi, \eta), y(\xi, \eta)) \tilde{q}_{ij,x}(x(\xi, \eta), y(\xi, \eta)) d\xi d\eta, \quad (5.23) \\ \tilde{B}_{ij} \tilde{q}_{ij,y} = \int_0^1 \int_0^1 \sqrt{a_{ij}(\xi, \eta)} \tilde{B}_{ij}(x(\xi, \eta), y(\xi, \eta)) \tilde{q}_{ij,y}(x(\xi, \eta), y(\xi, \eta)) d\xi d\eta,$$

where we use piecewise polynomial reconstructed functions \tilde{q} and a piecewise polynomial representations of the matrix valued functions. For a planar two-dimensional mapped grid cell, the area element \sqrt{a} is defined by

$$\sqrt{a} = \left| (c_{10}^1 + c_{11}^1 \eta)(c_{01}^2 + c_{11}^2 \xi) - (c_{01}^1 + c_{11}^1 \xi)(c_{10}^2 + c_{11}^2 \eta) \right|.$$

The coefficients $c_{10}, \dots, c_{11} \in \mathbb{R}^2$ are special cases of those detailed in §4.3, and can be obtained from those coefficients by setting ζ and the third component of \mathbf{X} equal to zero.

In order to define the fluctuations $\mathcal{A}^\pm \Delta q$ and $\mathcal{B}^\pm \Delta q$, we introduce $\mathbf{n}_{i\pm\frac{1}{2}j}$ and $\mathbf{n}_{i,j\pm\frac{1}{2}}$, the normal vectors at the interfaces $(i\pm\frac{1}{2}j)$ and $(i,j\pm\frac{1}{2})$. We define $A|_{\Psi}$ by replacing the matrix A in the one-dimensional formula of Section 5.1 by $\hat{A} = n^1 A + n^2 B$. Now we integrate the fluctuations over each grid cell interface using again the piecewise polynomial reconstructed values. For example we compute

$$\mathcal{A}^- \Delta q_{i+\frac{1}{2}j} = \int_0^1 \frac{1}{2} \left[\hat{A}|_{\Psi_{i+\frac{1}{2}j}}(\eta) - \alpha_{i+\frac{1}{2}j}(\eta) \mathbb{I} \right] \left(q_{i+\frac{1}{2}j}^+(\eta) - q_{i+\frac{1}{2}j}^-(\eta) \right) d\eta. \quad (5.24)$$

All the other fluctuations are computed analogously.

5.4. Limiting with respect to the derivative. As first pointed out by Rossmannith in [39], a special limiting is needed for the update of the magnetic potential in order to

avoid unphysical oscillation in derivatives of the potential and thus in the magnetic field. He proposed an extension of the limiting mechanism used in the wave propagation algorithm.

Here we describe a limiting strategy that can be used in combination with the update of the potential that is proposed in this paper. The strategy of limiting with respect to the derivative will be described for the 1D advection equation

$$q_{,t} + uq_{,x} = 0, \quad (5.25)$$

where $q : \mathbb{R} \times \mathbb{R}^+ \rightarrow \mathbb{R}$ is continuous but not necessarily continuously differentiable. The advection speed $u \in \mathbb{R}$ is assumed to be constant and we restrict to the case $u > 0$. We use the method introduced in Section 5.1 together with the third order accurate SSP-RK method to update the advected quantity q .

In order to limit the solution we add numerical viscosity¹ to the problem, i.e. instead of (5.25) we approximate an advection diffusion equation of the form

$$q_{,t} + uq_{,x} = \varepsilon(x) q_{,x,x}. \quad (5.26)$$

This scalar advection-diffusion equation can also be written as a system of first order equations

$$q_{,t} + uq_{,x} = \varepsilon(x) d_{,x}, \quad (5.27)$$

$$d - q_{,x} = 0. \quad (5.28)$$

Usually $\varepsilon(x)$ is chosen such that a thin layer is added near discontinuities in the solution itself while keeping the high order reconstruction away from the discontinuity (e.g., see [34]). We will change the definition of ε in such a way that additional viscosity is added near jumps in the derivative of the solution.

The artificial viscosity must satisfy the following requirements:

1. It should be small enough to satisfy the stability constraint

$$\frac{\varepsilon(x)\Delta t}{(\Delta x)^2} \leq \frac{1}{2}$$

of our explicit time-stepping method.

2. It should be large enough to avoid spurious oscillations in the derivative due to Gibbs phenomenon.
3. The artificial viscosity should not degrade the accuracy of the scheme for smooth solution structures.

To be able to handle all these requirements we define the viscosity in the following way:

$$\varepsilon(x) = \eta\alpha, \quad (5.29)$$

with

$$\eta = 0.2 \frac{(\Delta x)^2}{\Delta t}, \quad (5.30)$$

and

$$\alpha = \begin{cases} \frac{1}{2} [1 + \sin(\pi \Delta S - \frac{\pi}{2})] & S > \sigma_{ii}, \\ 0 & S \leq \sigma_{ii}, \end{cases} \quad (5.31)$$

¹In the context of the evolution of the magnetic potential in ideal MHD, the term *numerical viscosity* really refers to *numerical resistivity*.

where

$$S = \max(\sigma_{i i-1}, \sigma_{i i+1}), \quad \Delta S = |S - \sigma_{ii}|, \quad (5.32)$$

$$\sigma_{ik} = \frac{\lambda_{ik}}{((\Delta x)^4 + \Sigma_{ik})^e}, \quad \Sigma_{ik} = (\tilde{q}_{,x,x}(k)(\Delta x)^2)^2, \quad k \in (i-1, i, i+1).$$

The parameters are set to $\lambda_{i i-1} = \lambda_{i i+1} = 1$, $\lambda_{ii} = 1000$ and $e = 4$ in the test below. Note that we use a double index on the parameters λ and σ ; the logic behind this notation is that the first index denotes the current cell that is being considered and the second index denotes the cell to which the current cell is being compared. η is the maximum amount of viscosity that could be added and α is a smoothness indicator, with values between 0 and 1, such that α approaches 1 on very steep gradients in the derivative (i.e., steep second derivative), and α is 0 in smooth regions of the derivative. The idea behind this smoothness indicator is that we do not take any viscosity (large linear weight λ_{ii}), unless the second derivative in one of the neighbouring cells is much higher than in cell i , in which case we will add some viscosity depending on the difference of the smoothness measure σ_{ii} and the maximum of the smoothness measures in the neighbouring cells ($\sigma_{i i-1}, \sigma_{i i+1}$). This means that the parameter λ_{ii} controls how much the second derivatives have to differ, before adding any viscosity. We found that $\lambda_{ii} \in [10^1, 10^3]$ seem to give good results. From the form of the viscosity, it is clear that we do not obtain a further time step restriction due to the viscosity limiting. Taking the time step restriction into account, one could also choose $\eta = \mathcal{O}(\Delta x)$ empirically.

We now consider the 1D advection example that was first introduced in [39]. Consider (5.25) with $u = 1$ on the interval $0 \leq x \leq 1$ and double periodic boundary conditions. The initial data is the following piecewise linear function:

$$q(0, x) = \begin{cases} 0 & \text{if } x \leq 0.25, \\ (x - 0.25)/0.075 & \text{if } 0.25 \leq x \leq 0.4, \\ 2 & \text{if } 0.4 \leq x \leq 0.6, \\ (0.75 - x)/0.075 & \text{if } 0.6 \leq x \leq 0.75, \\ 0 & \text{if } 0.75 \leq x. \end{cases}$$

Note that $q(0, x)$ is continuous, but its first derivative is discontinuous. The challenge is to control oscillations in both $q(t, x)$ and $q_{,x}(t, x)$.

We compare the solution and its derivative as computed by two different limiters: (a) a standard WENO limiter that is essentially non-oscillatory in $q(t, x)$, but not necessarily in $q_{,x}(t, x)$, and (b) the proposed limiter as described above. For further details on the WENO limiting see Canestrelli et al. [12], Titarev et al. [44] and Tsoutsanis et al. [46]. Third order accurate average values of the derivatives $q_{,x}(t, x)$ are computed using

$$\frac{1}{\Delta x} \int_{x_{i-\frac{1}{2}}}^{x_{i+\frac{1}{2}}} q_{,x}(t, x) dx = \frac{1}{\Delta x} \left[q \left(t, x_{i+\frac{1}{2}} \right) - q \left(t, x_{i-\frac{1}{2}} \right) \right] \quad (5.33)$$

$$\approx \frac{1}{\Delta x} \left[\frac{1}{2} \left(q_{i+\frac{1}{2}}^-(t) + q_{i+\frac{1}{2}}^+(t) \right) - \frac{1}{2} \left(q_{i-\frac{1}{2}}^-(t) + q_{i-\frac{1}{2}}^+(t) \right) \right].$$

We use a CFL number of 0.7 in both simulations. The solution and its derivative at time $t = 1$ (i.e., after one revolution) are shown in Figure 5.1, where Panel (a) is the WENO limiter and Panel (b) is the proposed limiter. The approximation of $q(1, x)$ looks very similar in both cases. However, there are obvious differences in the computed results for $q_{,x}(t, x)$; the proposed limiter avoids spurious oscillations in $q_{,x}(t, x)$. In comparison with the TVD scheme

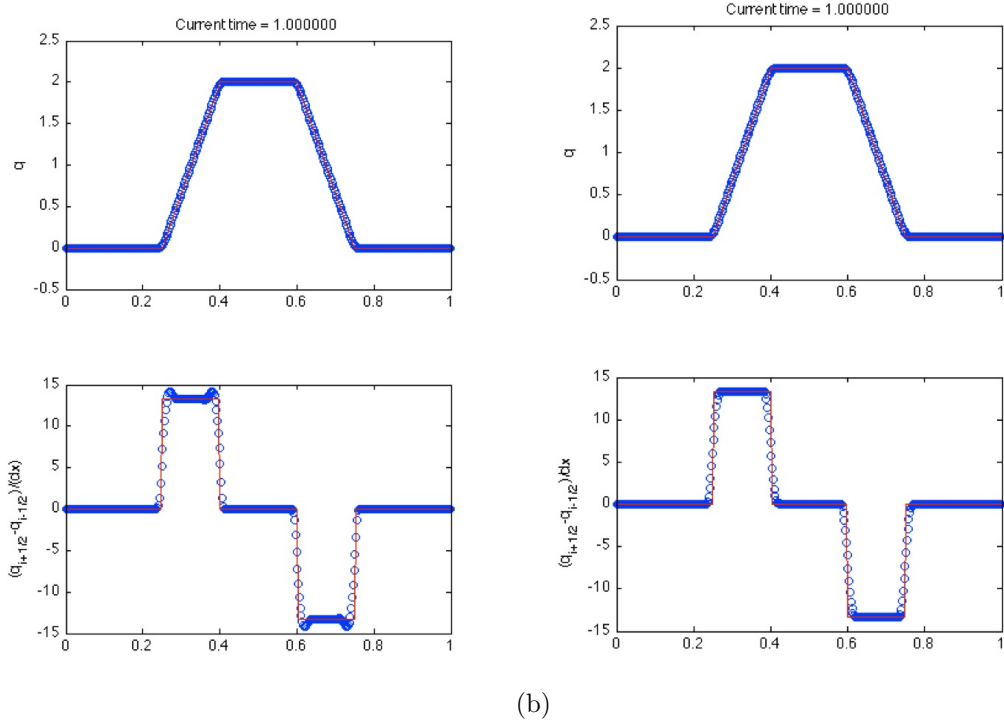


FIG. 5.1. The solution to the 1D advection equation and its derivative on a periodic domain after one revolution using the 3rd order algorithm. Panel (a) shows how standard WENO limiting performs on the solution, and Panel (b) shows how the limiter proposed in this work performs.

of [39] the limiting introduced here (which can also be used in a one-step scheme) seems to be slightly more diffusive. This however is a general problem if a method of lines approach is used instead of a Lax-Wendroff type method.

In the multidimensional case, we compute the smoothness indicator S by taking all neighboring grid cells into account that share a face, an edge or a corner point with the considered grid cell. For the computation of Σ , the second derivative of \tilde{q} is replaced by the Laplacian and $(\Delta x)^2$ is replaced by $(|C_{ij}|)$ in the two-dimensional case, and $(|C_{ijk}|)$ in the three-dimensional case. As characteristic length in the computation of η and σ (Δx in 1D), we use the length of the smallest edge of the considered grid cell in the multidimensional case. Denoting the characteristic length by Δs , we use $\eta = 0.5\Delta s$ in all MHD computations below and $\lambda_{i-1} = 1$, $\lambda_{i+1} = 1$, and $\lambda_{ii} = 10^3$ (see formulas in (5.32)).

6. The discretization of $\nabla \times \mathbf{A}$. During each stage of the constrained transport algorithm described in Section 3, we obtain the corrected magnetic field from taking the curl of the magnetic potential. In our previous work on CT schemes [26, 39], the cell average values of the magnetic field were computed using centered finite difference approximations. In order for the scheme developed in this work to be third order accurate both on Cartesian and mapped grids, we must generalize the central finite difference approach. We describe this generalization in this section.

We wish to compute a discrete version of the curl of the magnetic vector potential:

$$\mathbf{B} = \nabla \times \mathbf{A} = [A_{,y}^3 - A_{,z}^2, \quad A_{,z}^1 - A_{,x}^3, \quad A_{,x}^2 - A_{,y}^1]^T. \quad (6.1)$$

In particular, we wish to compute a third order accurate estimate of the cell average of \mathbf{B} . For example, using the divergence theorem, the cell average of the first component of the magnetic field, B^1 , in grid cell (i, j, k) can be expressed in the form

$$\begin{aligned} B_{ijk}^1 &= \frac{1}{|C_{ijk}|} \iiint_{C_{ijk}} (A_{,y}^3 - A_{,z}^2) dV \\ &= \frac{1}{|C_{ijk}|} \iiint_{C_{ijk}} \nabla \cdot \begin{pmatrix} 0 \\ A^3 \\ -A^2 \end{pmatrix} dV \\ &= \frac{1}{|C_{ijk}|} \oint_{\partial C_{ijk}} \begin{pmatrix} 0 \\ A^3 \\ -A^2 \end{pmatrix} \cdot \nu dA \\ &= \frac{1}{|C_{ijk}|} \oint_{\partial C_{ijk}} (A^3 \nu^2 - A^2 \nu^3) dA, \end{aligned} \quad (6.2)$$

where $\nu = (\nu^1, \nu^2, \nu^3) \in \mathbb{R}^3$ is the outward pointing unit normal vector along the boundary ∂C_{ijk} of the considered grid cell. The integrals over all the faces of a grid cell can be evaluated in computational space as discussed in Section 4.3. Using the definition of the surface normal vector \mathbf{n} and the determinant a of the mapping as defined for the grid cell interfaces in Section 4.3, we obtain

$$\begin{aligned} B_{ijk}^1 &= \frac{1}{|C_{ijk}|} \sum_{\pm=+,-} \left\{ \pm \int_0^1 \int_0^1 \left((A^3 n^2(\eta, \zeta) - A^2 n^3(\eta, \zeta)) \sqrt{a(\eta, \zeta)} \right)_{i \pm \frac{1}{2}, j, k} d\eta d\zeta \right. \\ &\quad \pm \int_0^1 \int_0^1 \left((A^3 n^2(\xi, \zeta) - A^2 n^3(\xi, \zeta)) \sqrt{a(\xi, \zeta)} \right)_{i, j \pm \frac{1}{2}, k} d\xi d\zeta \\ &\quad \left. \pm \int_0^1 \int_0^1 \left((A^3 n^2(\xi, \eta) - A^2 n^3(\xi, \eta)) \sqrt{a(\xi, \eta)} \right)_{i, j, k \pm \frac{1}{2}} d\xi d\eta \right\}. \end{aligned} \quad (6.3)$$

In order to evaluate the surface integral in (6.3), we first replace the integrals with a Gaussian quadrature rule of the appropriate degree of precision, then we reconstruct A^2 and A^3 on the grid cell boundaries at each of the quadrature points using the piecewise polynomial reconstruction of \mathbf{A} . To be more precise, at each of these quadrature points we take the value of \mathbf{A} to be the average of the reconstructed values from the two grid cells that share a face. We note that this discretization leads to a conservative update of the magnetic field. For a smooth magnetic potential the average of the reconstructed values agrees with the correct interface value of the magnetic potential up to the order used in the reconstruction. The computation of the cell averages of B^2 and B^3 can be done in an analogous way using

$$\begin{aligned} B_{ijk}^2 &= \frac{1}{|C_{ijk}|} \oint_{\partial C_{ijk}} (A^1 \nu^3 - A^3 \nu^1) dA \\ B_{ijk}^3 &= \frac{1}{|C_{ijk}|} \oint_{\partial C_{ijk}} (A^2 \nu^1 - A^1 \nu^2) dA. \end{aligned}$$

CLAIM 6.1. *The constrained transport method as described in this work locally conserves (and therefore also globally conserves) the magnetic field, \mathbf{B} , from one Runge-Kutta stage to the next.*

Proof. Without loss of generality consider a single Euler step (i.e., a single stage in the SSP time-stepping scheme) on the magnetic field:

$$\begin{aligned}\mathbf{B}^{n+1} &= \nabla \times \mathbf{A}^{n+1} = \nabla \times (\mathbf{A}^n + \Delta t \mathbf{E}^n) \\ &= \mathbf{B}^n + \Delta t \nabla \times \mathbf{E}^n = \mathbf{B}^n + \Delta t \nabla \cdot \left([\epsilon_{ijk} E^k]^n \right).\end{aligned}\tag{6.4}$$

The divergence of the tensor $[\epsilon_{ijk} E^k]$ is computed via surface integrals of the form (6.3), where \mathbf{A} is replaced with \mathbf{E} . The values of $\mathbf{E} = (\nabla \times \mathbf{A}) \times \mathbf{u}$ are computed from constrained transport as described in Section 5 and then averaged onto appropriate Gaussian quadrature points on each face. In particular, note that the same values of \mathbf{E} are used to update the cell average of $\nabla \cdot ([\epsilon_{ijk} E^k])$ on either side of the face. Therefore, we are guaranteed that the discrete magnetic field is locally conserved over each Euler time step. \square

7. Numerical Results. Several numerical examples on Cartesian and mapped grids are shown in this section. These examples are used to both verify the third-order accuracy in space and time, as well as the shock-capturing ability of the scheme proposed in this work.

7.1. Smooth Alfvén wave problem. We consider two variants of the so-called smooth Alfvén wave problem: a (1) 2.5D variant and (2) 3D variant. Note that the term 2.5D here refers to the case of a two-dimensional computational domain, but with vector unknowns \mathbf{u} and \mathbf{B} that have three non-trivial components. In 2.5D for the magnetic potential we solve equation (2.23) with $\mathbf{A}_{,z} = 0$ using the method described in Section 5.

7.1.1. 2.5D problem. In this case the analytical solution consists of a sinusoidal wave propagating at constant speed in direction $\mathbf{n} = (\cos \phi, \sin \phi, 0)$ without changing shape. We use $\phi = \arctan(0.5)$ and solve in the domain $(x, y) \in [0, (\cos \phi)^{-1}] \times [0, (\sin \phi)^{-1}]$ with double periodic boundary conditions. The initial values of all components are described in [26]. Similar problems were also considered by Rossmannith [39] and Tóth [42].

In Table 7.1 we show the results of a numerical convergence study of the new constrained transport algorithm on a 2D Cartesian grid. We obtain full third order convergence rates in all conserved quantities, as well as all the magnetic vector potential components.

We have also computed this test problem on a mapped grid, which is a scaled version of a grid from Colella et al. [15]. The mapping has the form

$$T(x_c, y_c) = \begin{pmatrix} x_c \\ y_c \end{pmatrix} + \beta \sin \left(\frac{2\pi x_c}{L} \right) \sin \left(\frac{2\pi y_c}{M} \right) \begin{pmatrix} 1 \\ 1 \end{pmatrix},\tag{7.1}$$

where (x_c, y_c) are the coordinates in computational space, $\beta \in \mathbb{R}$ is a parameter which determines the smoothness of the grid, and L, M describe the length of the domain in the x and y direction, respectively. Here we use $\beta = 0.1$, $L = (\cos \phi)^{-1}$ and $M = (\sin \phi)^{-1}$. The mapped grid is shown in Panel (a) of Figure 7.1. Table 7.2 confirms the third order convergence rate also for the mapped grid computation. Note that the error on the mapped grid is only slightly larger than the error on the Cartesian grid. However, we note that the least squares approach that we used for the piecewise polynomial reconstruction leads to the correct order only on grids that do not have highly stretched cells (e.g., see Petrovskaya [35]).

7.1.2. 3D problem. Next we have performed a convergence study for the 3D smooth Alfvén wave problem on a Cartesian grid. The results, which again confirm the third order convergence rate, are presented in Table 7.3. The initial values and the computational domain for this problem are described in [26].

| | ρ | ρu^1 | ρu^2 | ρu^3 | \mathcal{E} |
|------------------|------------------------|------------------------|------------------------|------------------------|------------------------|
| 32×64 | 5.128×10^{-4} | 2.413×10^{-4} | 6.059×10^{-4} | 5.142×10^{-4} | 1.301×10^{-4} |
| 64×128 | 6.495×10^{-5} | 3.097×10^{-5} | 7.548×10^{-5} | 6.469×10^{-5} | 1.653×10^{-5} |
| 128×256 | 8.150×10^{-6} | 3.924×10^{-6} | 9.412×10^{-6} | 8.099×10^{-6} | 2.075×10^{-6} |
| 256×512 | 1.020×10^{-6} | 4.933×10^{-7} | 1.176×10^{-6} | 1.014×10^{-6} | 2.599×10^{-7} |
| EOC | 2.998 | 2.992 | 3.000 | 2.998 | 2.997 |

| | B^1 | B^2 | B^3 |
|------------------|------------------------|------------------------|------------------------|
| 32×64 | 2.877×10^{-4} | 5.754×10^{-4} | 5.123×10^{-4} |
| 64×128 | 3.583×10^{-5} | 7.166×10^{-5} | 6.437×10^{-5} |
| 128×256 | 4.464×10^{-6} | 8.928×10^{-6} | 8.057×10^{-6} |
| 256×512 | 5.581×10^{-7} | 1.116×10^{-6} | 1.008×10^{-6} |
| EOC | 3.000 | 3.000 | 2.999 |

| | A^1 | A^2 | A^3 |
|------------------|------------------------|------------------------|------------------------|
| 32×64 | 3.583×10^{-5} | 6.921×10^{-5} | 1.053×10^{-4} |
| 64×128 | 4.489×10^{-6} | 8.628×10^{-6} | 1.327×10^{-5} |
| 128×256 | 5.626×10^{-7} | 1.076×10^{-6} | 1.661×10^{-6} |
| 256×512 | 7.041×10^{-8} | 1.344×10^{-7} | 2.077×10^{-7} |
| EOC | 2.998 | 3.000 | 2.999 |

TABLE 7.1

Convergence study of the 2.5D smooth Alfvén wave problem on a Cartesian mesh. The tables show the L_1 -error at time $t = 1$ in the different physical quantities computed using the constrained transport algorithm. The experimental order of convergence (EOC) is computed by comparing the error for the two finest grids. All simulations are performed using a CFL number of 0.5.

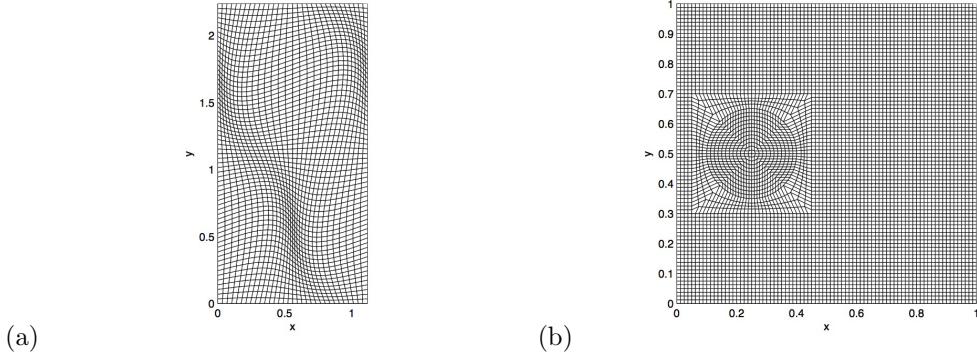


FIG. 7.1. Shown in this figure are the mapped grids used in (a) the convergence study of the smooth Alfvén wave problem and (b) the cloud-shock interaction problem.

7.2. 2.5D shock tube problem on mapped grids. Next we consider a 1D shock tube problem on a scaled versions of the 2D mapped grid given by (7.1). This example demonstrates the performance of the new CT method on shocks not moving along grid lines.

The computational domain is the square $[-0.7, 0.7] \times [-0.7, 0.7]$. In order to avoid inaccuracies at the boundary of the domain, we restrict the mapping to the area $-0.6 \leq x_c, y_c \leq 0.6$. The rest of the mesh is Cartesian. We set $L = M = 1.2$ and use different values of β .

| | ρ | ρu_1 | ρu_2 | ρu_3 | \mathcal{E} |
|------------------|------------------------|------------------------|------------------------|------------------------|------------------------|
| 32×64 | 1.975×10^{-3} | 7.167×10^{-4} | 1.223×10^{-3} | 7.711×10^{-4} | 5.230×10^{-4} |
| 64×128 | 2.631×10^{-4} | 9.756×10^{-5} | 1.557×10^{-4} | 9.745×10^{-5} | 6.955×10^{-5} |
| 128×256 | 3.333×10^{-5} | 1.245×10^{-5} | 1.953×10^{-5} | 1.222×10^{-5} | 8.820×10^{-6} |
| EOC | 2.981 | 2.970 | 2.996 | 2.996 | 2.980 |

| | B^1 | B^2 | B^3 |
|------------------|------------------------|------------------------|------------------------|
| 32×64 | 4.827×10^{-4} | 9.735×10^{-4} | 9.483×10^{-4} |
| 64×128 | 6.014×10^{-5} | 1.213×10^{-4} | 1.219×10^{-4} |
| 128×256 | 7.511×10^{-6} | 1.513×10^{-5} | 1.534×10^{-5} |
| EOC | 3.001 | 3.002 | 2.990 |

| | A^1 | A^2 | A^3 |
|------------------|------------------------|------------------------|------------------------|
| 32×64 | 7.355×10^{-5} | 1.260×10^{-4} | 1.749×10^{-4} |
| 64×128 | 9.358×10^{-6} | 1.595×10^{-5} | 2.216×10^{-5} |
| 128×256 | 1.175×10^{-6} | 2.000×10^{-6} | 2.776×10^{-6} |
| EOC | 2.994 | 2.996 | 2.997 |

TABLE 7.2

Convergence study of the 2.5D smooth Alfvén wave problem on a mapped grid. The tables show the L_1 -error at time $t = 1$ in the different physical quantities computed using the constrained transport algorithm. The experimental order of convergence (EOC) is computed by comparing the error for the two finest grids. All simulations are performed using a CFL number of 0.5.

| | ρ | ρu_1 | ρu_2 | ρu_3 | \mathcal{E} |
|----------------------------|------------------------|------------------------|------------------------|------------------------|------------------------|
| $16 \times 32 \times 32$ | 2.055×10^{-3} | 9.992×10^{-4} | 1.716×10^{-3} | 1.911×10^{-3} | 5.133×10^{-4} |
| $32 \times 64 \times 64$ | 2.684×10^{-4} | 1.343×10^{-4} | 2.213×10^{-4} | 2.532×10^{-4} | 6.611×10^{-5} |
| $64 \times 128 \times 128$ | 3.419×10^{-5} | 1.679×10^{-5} | 2.764×10^{-5} | 3.110×10^{-5} | 8.701×10^{-6} |
| EOC | 2.973 | 3.000 | 3.001 | 3.025 | 2.926 |

| | L_1 Error in B^1 | L_1 Error in B^2 | L_1 Error in B^3 |
|----------------------------|------------------------|------------------------|------------------------|
| $16 \times 32 \times 32$ | 1.231×10^{-3} | 1.805×10^{-3} | 1.778×10^{-3} |
| $32 \times 64 \times 64$ | 1.581×10^{-4} | 2.304×10^{-4} | 2.296×10^{-4} |
| $64 \times 128 \times 128$ | 1.957×10^{-5} | 2.869×10^{-5} | 2.818×10^{-5} |
| EOC | 3.014 | 3.006 | 3.026 |

| | L_1 Error in A^1 | L_1 Error in A^2 | L_1 Error in A^3 |
|----------------------------|------------------------|------------------------|------------------------|
| $16 \times 32 \times 32$ | 1.588×10^{-4} | 2.933×10^{-4} | 2.869×10^{-4} |
| $32 \times 64 \times 64$ | 2.340×10^{-5} | 3.642×10^{-5} | 3.671×10^{-5} |
| $64 \times 128 \times 128$ | 2.550×10^{-6} | 4.780×10^{-6} | 4.617×10^{-6} |
| EOC | 3.198 | 2.930 | 2.991 |

TABLE 7.3

Convergence study of the 3D smooth Alfvén wave problem on a Cartesian grid. The tables show the L_1 -error at time $t = 1$ in the different physical quantities computed using the constrained transport algorithm. The experimental order of convergence (EOC) is computed by comparing the error for the two finest grids. All simulations are performed using a CFL number of 0.6.

The Riemann initial data have the form

$$\begin{aligned} & (\rho, u^1, u^2, u^3, p, B^1, B^2, B^3)(0, \mathbf{x}) \\ &= \begin{cases} \left(1.08, 1.2, 0.01, 0.5, 0.95, \frac{2}{\sqrt{4\pi}}, \frac{3.6}{\sqrt{4\pi}}, \frac{2}{\sqrt{4\pi}} \right) & \text{if } x < 0, \\ \left(1, 0, 0, 0, 1, \frac{2}{\sqrt{4\pi}}, \frac{4}{\sqrt{4\pi}}, \frac{2}{\sqrt{4\pi}} \right) & \text{if } x \geq 0. \end{cases} \end{aligned} \quad (7.2)$$

As the initial condition for the magnetic potential we use

$$(A^1, A^2, A^3)(0, \mathbf{x}) = (0, xB^3, yB^1 - xB^2). \quad (7.3)$$

We utilize zeroth order extrapolation on all boundaries for the MHD variables and linear extrapolation for the magnetic potential. Shown is a comparison of scatter plots for the magnetic field components along the x -axis.

In Figure 7.2, we show results for the magnetic field components using the new CT method. Here we compare results for different grids, namely a Cartesian grid and two different versions of the mapped grid obtained by setting the parameter β to either 1/50 or 1/15. For all simulations we used grids with 200×200 mesh cells. Note that for the mapped grid computations the solution structure, moving only in x -direction, is not aligned with the grid. It has been observed previously that this leads to unphysical oscillations, see [26, 32]. A numerical convergence study for B^1 on mapped grids with different resolution showed that the error in the L_1 norm decreases with a rate of about 1/3. By introducing more numerical viscosity (i.e. decreasing the value of λ_{ii}) these oscillations can be slightly reduced. However, they could not be avoided. Here we show results for $\lambda_{ii} = 10^3$. The solid lines in these plots are obtained by computing solutions of the one-dimensional Riemann problem on a very fine equidistant mesh.

7.3. Cloud-shock interaction problem. Next we present numerical results of the proposed method for a cloud-shock interaction problem. Again we consider 3D and 2.5D variants of this problem.

7.3.1. 3D problem. The initial conditions consist of a shock that is located at $x = 0.05$, with

$$\begin{aligned} & (\rho, u^1, u^2, u^3, p, B^1, B^2, B^3)(0, \mathbf{x}) \\ &= \begin{cases} (3.86859, 11.2536, 0, 0, 167.345, 0, 2.1826182, -2.1826182) & \text{if } x < 0.05, \\ (1, 0, 0, 0, 1, 0, 0.56418958, 0.56418958) & \text{if } x \geq 0.05, \end{cases} \end{aligned} \quad (7.4)$$

and a spherical cloud of density $\rho = 10$ with radius $r = 0.15$ centered at $(0.25, 0.5, 0.5)$. The cloud is in hydrostatic equilibrium with the fluid to the right of the shock. The initial conditions for the magnetic potential are given by

$$\mathbf{A}(0, \mathbf{x}) = \begin{cases} (2.1826182 y, 0, -2.1826182(x - 0.05))^T & \text{if } x < 0.05, \\ (-0.56418958 y, 0, 0.56418956(x - 0.05))^T & \text{if } x \geq 0.05. \end{cases} \quad (7.5)$$

The computational domain is the unit cube. Inflow boundary conditions are used at the left side and outflow boundary conditions are used at all other sides. Without the constrained transport step the method would fail to compute the solution structure. In Figure 7.3 we present results of a computation with the three-dimensional method proposed in this paper. Compare also with [26], where this problem was computed with our previous approach.

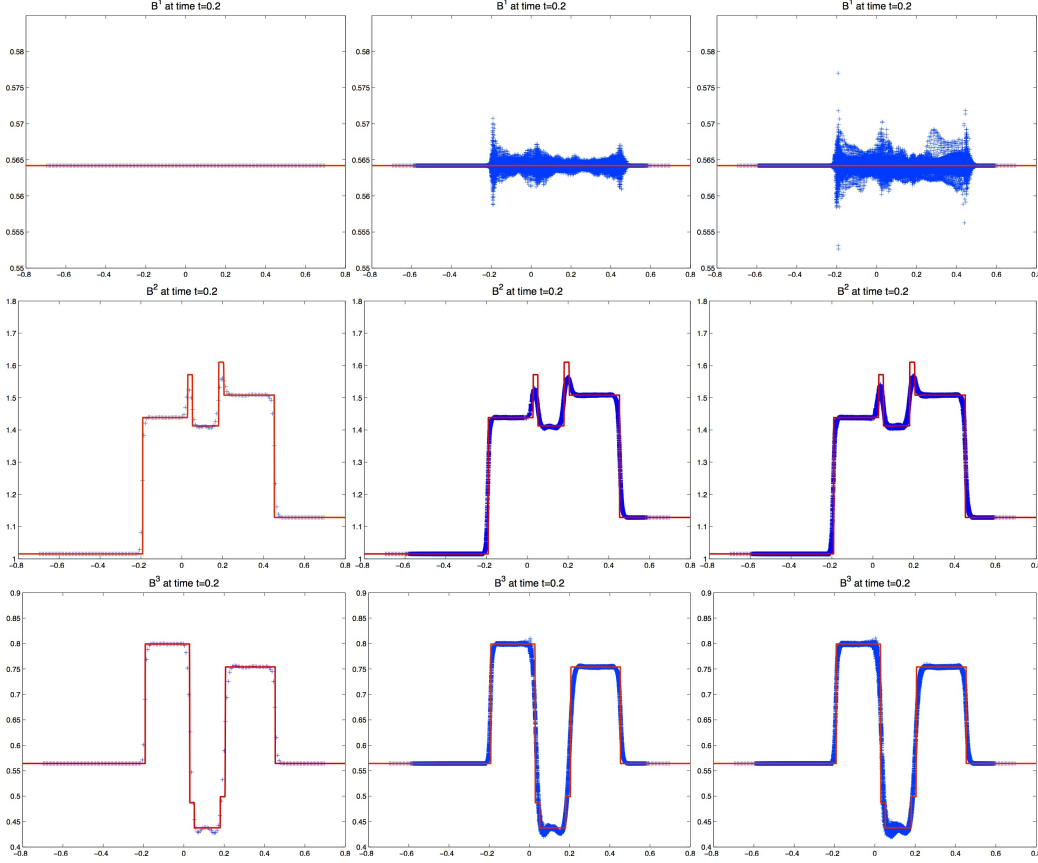


FIG. 7.2. Shown are the magnetic field components for the shock tube problem at $t = 0.2$. The left column shows the results for a Cartesian grid computation; the middle column shows results on a mapped grid which is a small perturbation of the Cartesian grid (using $\beta = 1/50$); the right column shows results on a mapped grid which is a larger perturbation of the Cartesian grid (using $\beta = 1/15$).

7.3.2. 2.5D problem. We also studied the cloud-shock interaction problem in the 2.5D case. The initial values are taken from the 3D test problem by setting $z = 0.5$. In the 2.5D case we show results for B^3 as computed by the new constrained transport algorithm that updates all three components of the magnetic field. The results compare well with those obtained by our previous approach [26] and also with the results from the 2D unsplit method of [39] in which only B^1 and B^2 are updated by a constrained transport method. We compute the solution both on a Cartesian grid as well as on a mapped grid. For the mapped grid computation we use a grid of the form shown in Panel (b) of Figure 7.1. This is a small modification of a grid with circular inclusion discussed in [11]. The initial cloud position is inside the circular region of the mapped grid. The results on both grids compare well, although the solution structure is slightly sharper resolved on the Cartesian mesh (see Figure 7.4).

8. Conclusions. In this work we developed a finite volume method for solving the 2D and 3D ideal MHD equations on both Cartesian and logically Cartesian mapped grids. The scheme is a method of lines that is based on a finite volume discretization in space coupled with a strong-stability-preserving Runge-Kutta time stepping method. By using this method of lines discretization, we were able to construct a third-order accurate algorithm for the MHD

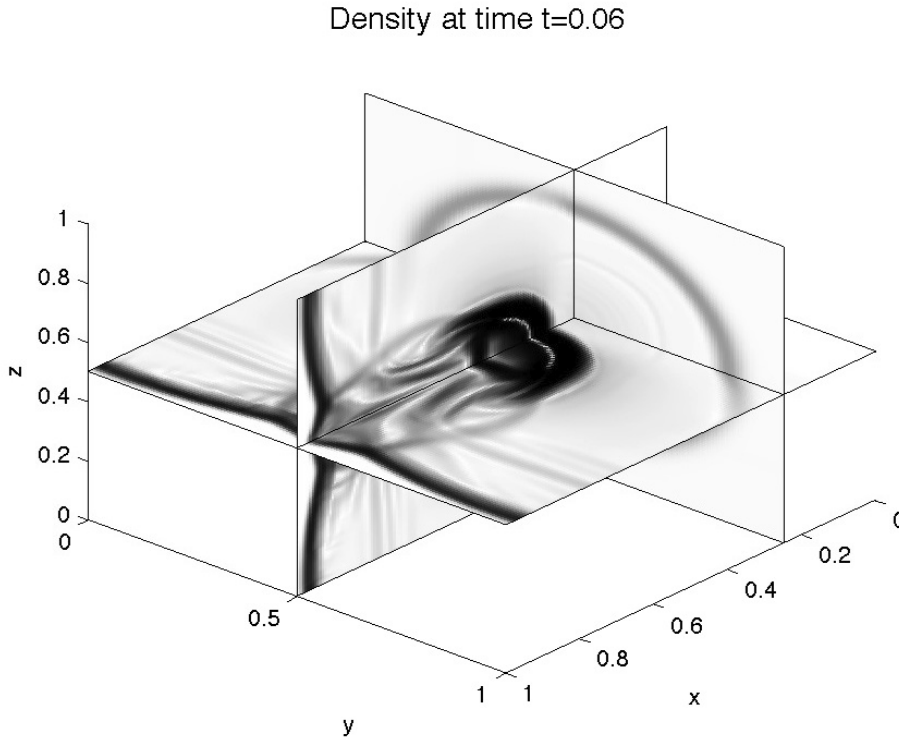


FIG. 7.3. This figure shows the density at time $t = 0.06$ on a three-dimensional Cartesian grid using $150 \times 150 \times 150$ mesh cells. For this simulation we used a 2nd order version of the proposed algorithm.

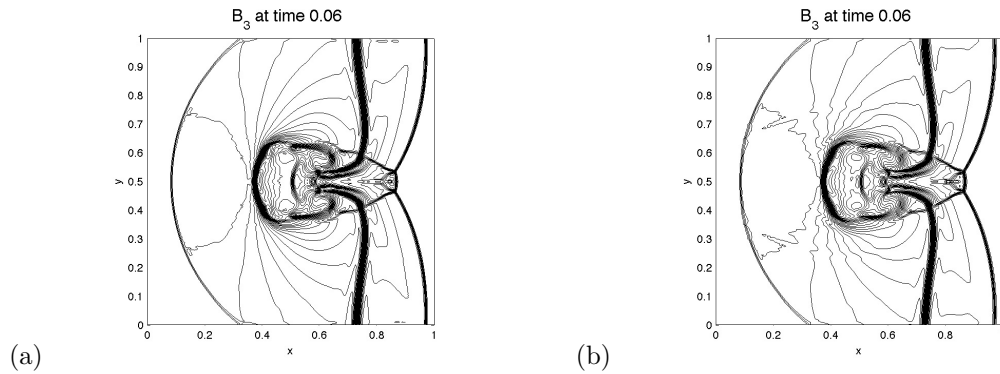


FIG. 7.4. The 3rd component of the magnetic field at time $t = 0.06$ (a) on a 256×256 Cartesian grid and (b) on the mapped grid shown in Figure 7.1 (right) using the 3rd order version of the algorithm. Here the 2.5 dimensional problem was implemented in such a way that all three components of the magnetic field were updated in the constrained transport step.

equations. In order to control errors in the divergence of the magnetic field we developed a novel constrained transport approach that couples to the finite volume discretization. Our constrained transport methodology allowed us to overcome two important difficulties: (1) the evolution equation for the magnetic potential is only weakly hyperbolic, and (2) standard

limiters applied to the magnetic potential do not adequately control unphysical oscillations in the magnetic field.

The method described in this work is based on the following procedure that is carried out during each Runge-Kutta stage:

1. Update the MHD variables without regard for controlling discrete $\nabla \cdot \mathbf{B}$ errors. The updated magnetic field in this step is the *predicted* magnetic field. This step is carried out with the finite volume schemes described in Section 4.
2. Update the magnetic vector potential by solving a weakly hyperbolic vector transport equation. This transport equation is simply the induction equation with ideal Ohm's law, but written in potential form using the Weyl gauge. This step is carried out with the non-conservative finite volume schemes described in Section 5. Special artificial resistivity limiters described in Section 5.4 are used in this step to simultaneously control unphysical oscillations in the magnetic potential and the magnetic field.
3. Define the *corrected* magnetic field as the result of taking the discrete curl of the updated magnetic vector potential. The precise form of the discrete curl operation is described in Section 6.

The resulting scheme was applied to several 2.5D and 3D test cases on both Cartesian and mapped grids. These test cases demonstrated two important features: (1) we are able to obtain full third-order accuracy on smooth problems and (2) we are able to accurately capture shock waves.

Finally we note that although there are some free parameters required in the definition of the artificial resistivity added in the magnetic vector potential equation update, we have found parameter values that seem to robustly work for a large class of problems. In all the simulations presented in this work we have stuck to these same parameter values. Experimentation with the λ_{ii} parameter in (5.32) shows that one can slightly increase or reduce the amount of artificial resistivity, but that for a broad range of λ_{ii} the results are qualitatively the same.

Acknowledgements. This work was supported in part by the DFG through FOR1048 and the NSF grants DMS-0711885 and DMS-1016202.

REFERENCES

- [1] D. Bale, R.J. LeVeque, S. Mitran, and J.A. Rossmannith. A wave propagation method for conservation laws and balance laws with spatially varying flux functions. *SIAM J. Sci. Comput.*, 24:955–978, 2002.
- [2] D.S. Balsara. Second-order-accurate schemes for magnetohydrodynamics with divergence-free reconstruction. *Astrophys. J. Suppl.*, 151:149–184, 2004.
- [3] D.S. Balsara and J. Kim. A comparison between divergence-cleaning and staggered-mesh formulations for numerical magnetohydrodynamics. *Astrophys. J.*, 602:1079–1090, 2004.
- [4] D.S. Balsara and D. Spicer. A staggered mesh algorithm using high order Godunov fluxes to ensure solenoidal magnetic fields in magnetohydrodynamic simulations. *J. Comp. Phys.*, 149(2):270–292, 1999.
- [5] T. Barth and P. Frederickson. Higher order solution of the Euler equations on unstructured grids using quadratic reconstruction. *AIAA-90-0013*, 1990.
- [6] T.J. Barth. Numerical methods for gasdynamic systems on unstructured meshes. *Lecture Notes in Computational Science and Engineering*, 5:195–285, 1998.
- [7] T.J. Barth. On the role of involutions in the discontinuous Galerkin discretization of Maxwell and magnetohydrodynamic systems. In *IMA Volume on Compatible Spatial Discretizations*, volume 142. Springer-Verlag, 2005.
- [8] J.U. Brackbill and D.C. Barnes. The effect of nonzero $\nabla \cdot b$ on the numerical solution of the magnetohydrodynamic equations. *J. Comp. Phys.*, 35:426–430, 1980.

- [9] J.U. Brackbill and D.C. Barnes. The effect of nonzero $\nabla \cdot b$ on the numerical solution of the magnetohydrodynamic equations. *J. Comput. Phys.*, 136:446–466, 1997.
- [10] D. Calhoun and R.J. LeVeque. An accuracy study of mesh refinement on mapped grids. *Lecture Notes in Computational Science and Engineering*, 41:91–102, 2003.
- [11] D.A. Calhoun, C. Helzel, and R.J. LeVeque. Logically rectangular grids and finite volume methods for PDEs in circular and spherical domains. *SIAM Review*, 50(4):723–752, 2008.
- [12] A. Canestrelli, A. Siviglia, M. Dumbser, and E.F. Toro. Well-balanced high-order centered schemes for non-conservative hyperbolic systems. Applications to shallow water equations with fixed and mobile bed. *Advances in Water Resources*, 32:834–844, 2009.
- [13] M.J. Castro, A. Pardo, C. Parés, and E.F. Toro. On some fast well-balanced first order solvers for nonconservative systems. *Mathematics of Computation*, 79(S 0025-5718(09)02317-5), 2010.
- [14] F.F. Chen. *Introduction to Plasma Physics and Controlled Fusion*. Plenum Press, 1984.
- [15] P. Colella, M. Dorr, J. Hittinger, and D.F. Martin. High-order finite volume methods in mapped coordinates. *J. Comput. Phys.*, 230:2952–2976, 2011.
- [16] C. Dafermos. *Hyperbolic Conservation Laws in Continuum Physics*. Springer, 2010.
- [17] W. Dai and P.R. Woodward. A simple finite difference scheme for multidimensional magnetohydrodynamic equations. *J. Comp. Phys.*, 142(2):331–369, 1998.
- [18] A. Dedner, F. Kemm, D. Kröner, C.-D. Munz, T. Schnitzer, and M. Wessenberg. Hyperbolic divergence cleaning for the MHD equations. *J. Comput. Phys.*, 175:645–673, 2002.
- [19] M. Dumbser, A. Hidalgo, M. Castro, C. Pares, and E.F. Toro. FORCE schemes on unstructured meshes II: Non-conservative hyperbolic systems. *Comput. Methods Appl. Mech. Engrg.*, 199:625–647, 2010.
- [20] C. Evans and J.F. Hawley. Simulation of magnetohydrodynamic flow: A constrained transport method. *Astrophys. J.*, 332:659–677, 1988.
- [21] M. Fey and M. Torrilhon. A constrained transport upwind scheme for divergence-free advection. In T.Y. Hou and E. Tadmor, editors, *Hyperbolic Problems: Theory, Numerics, and Applications*, pages 529–538. Springer, 2003.
- [22] S.K. Godunov. Symmetric form of the magnetohydrodynamic equations. *Numerical Methods for Mechanics of Continuum Medium*, 1:26–34, 1972.
- [23] T.I. Gombosi. *Physics of the Space Environment*. Cambridge University Press, 1998.
- [24] S. Gottlieb, D. Ketcheson, and C.W. Shu. *Strong Stability Preserving Runge-Kutta and Multistep Time Discretizations*. World Scientific, 2011.
- [25] S. Gottlieb, C.W. Shu, and E. Tadmor. Strong stability-preserving high-order time discretization methods. *SIAM Review*, 43(1):89–112, 2001.
- [26] C. Helzel, J. Rossmanith, and B. Taetz. An unstaggered constrained transport method for the 3d ideal magnetohydrodynamic equations. *J. Comp. Phys.*, 230:3803–3829, 2011.
- [27] D.I. Ketcheson, M. Parsant, and R.J. LeVeque. High-order wave propagation algorithms for general hyperbolic problems, 2011. submitted.
- [28] R.J. LeVeque. Wave propagation algorithms for multidimensional hyperbolic systems. *J. Comput. Phys.*, 131:327–353, 1997.
- [29] R.J. LeVeque. *Finite Volume Methods for Hyperbolic Problems*. Cambridge University Press, 2002.
- [30] P. Londrillo and L. Del Zanna. High-order upwind schemes for multidimensional magnetohydrodynamics. *Astrophys. J.*, 530:508–524, 2000.
- [31] P. Londrillo and L. Del Zanna. On the divergence-free condition in Godunov-type schemes for ideal magnetohydrodynamics: the upwind constrained transport method. *J. Comp. Phys.*, 195:17–48, 2004.
- [32] A. Mignone and P. Tzeferacos. A second-order unsplit Godunov scheme for cell-centered MHD: The CTU-GLM scheme. *J. Comp. Phys.*, 229:2117–2138, 2010.
- [33] G.K. Parks. *Physics of Space Plasmas: An Introduction*. Addison-Wesley, 1991.
- [34] P.O. Persson and J. Peraire. Sub-cell shock capturing for discontinuous galerkin methods. *AIAA-2006-0112*, 2006.
- [35] N. B. Petrovskaya. The accuracy of least-square approximation on highly stretched meshes. *Int. J. Comput. Meth.*, 5:449–462, 2008.
- [36] K.G. Powell. An approximate Riemann solver for magnetohydrodynamics (that works in more than one dimension). Technical Report 94-24, ICASE, Langley, VA, 1994.
- [37] K.G. Powell, P.L. Roe, T.J. Linde, T.I. Gombosi, and D.L. De Zeeuw. A solution-adaptive upwind scheme for ideal magnetohydrodynamics. *J. Comp. Phys.*, 154:284–309, 1999.
- [38] P.L. Roe and D. Balsara. Notes on the eigensystem of magnetohydrodynamics. *SIAM Appl. Math.*, 56:57–67, 1996.
- [39] J.A. Rossmanith. An unstaggered, high-resolution constrained transport method for magnetohydrodynamic flows. *SIAM J. Sci. Comp.*, 28:1766–1797, 2006.
- [40] D.S. Ryu, F. Miniati, T.W. Jones, and A. Frank. A divergence-free upwind code for multidimensional magnetohydrodynamic flows. *Astrophys. J.*, 509(1):244–255, 1998.

- [41] H. De Sterck. Multi-dimensional upwind constrained transport on unstructured grids for “shallow water” magnetohydrodynamics. In *Proceedings of the 15th AIAA Computational Fluid Dynamics Conference, Anaheim, California*, page 2623. AIAA, 2001.
- [42] G. Tóth. The $\nabla \cdot B = 0$ constraint in shock-capturing magnetohydrodynamics codes. *J. Comp. Phys.*, 161:605–652, 2000.
- [43] E. Tadmor. Entropy stability theory for difference approximations of nonlinear conservation laws and related time-dependent problems. *Acta Numerica*, 12:451–512, 2003.
- [44] V.A. Titarev, P. Tsoutsanis, and D. Drikakis. WENO schemes for mixed-element unstructured meshes. *Commun. Comput. Phys.*, 8(3):585–609, 2010.
- [45] M. Torrilhon. Locally divergence-preserving upwind finite volume schemes for magnetohydrodynamics. *SIAM J. Sci. Comp.*, 26:1166–1191, 2005.
- [46] P. Tsoutsanis, V.A. Titarev, and D. Drikakis. WENO schemes on arbitrary mixed-element unstructured meshes in three space dimensions. *J. Comput. Phys.*, 230:1585–1601, 2011.
- [47] O.V. Ushakova. Conditions of nondegeneracy of three-dimensional cells. a formula of a volume of cells. *SIAM J. Sci. Comput.*, 23:1274–1290, 2001.
- [48] K. Yee. Numerical solutions of initial boundary value problems involving Maxwell’s equations in isotropic media. *IEEE Transactions on Antennas and Propagation*, AP-14:302–307, 1966.